Alma Mater Studiorum - Università di Bologna

DOTTORATO DI RICERCA IN

AUTOMOTIVE PER UNA MOBILITÀ INTELLIGENTE

Ciclo 34

Settore Concorsuale: 09/F1 - CAMPI ELETTROMAGNETICI

Settore Scientifico Disciplinare: ING-INF/02 - CAMPI ELETTROMAGNETICI

AUTOMOTIVE ANTENNAS FOR V2X COMMUNICATIONS

Presentata da: Stefano Lenzini

Coordinatore Dottorato

Nicolò Cavina

Supervisore

Luca Vincetti

Co-supervisore

Stefano Selleri

Esame finale anno 2022

Contents

List of Figures

List of Tables

Abstract

The main topic of this thesis is about the design and prototyping of automotive antennas that allows Vehicle to Everything (V2X) communications, that is the communication between the vehicle and all what else is relevant. In particular 5G will be an enabling technology for these communications.

Vehicular connectivity is a mandatory feature in nowadays car. Typical applications are that one related to the infotainment, i.e. radio or mobile telephone, or security ones, i.e. radars. The antennas that support this type of communications can be divided in two frequency range: the sub-6GHz range and the millimeter wave (mmW) range. Also the 5G standard can be divided in this two frequency ranges. In this work different automotive antennas solutions are presented for both the frequency bands.

For the sub-6GHz range two different antennas are presented: a tin sheet 5G-sub6 radiating element and a complete 5G-GNSS-V2X shark fin module. For the mmW frequency band, an automotive PCB planar solution is presented. Since these frequencies are a novelty for the automotive market, satellite communications (SatCom) field has been considered. In SatCom applications mmW solutions are a well-established technology. Thus, also mmW antennas solutions for SatCom applications are here presented.

Chapter 1

Introduction

V2X is defined as the communication between a vehicle and all what else is relevant. For example, we can have V2I Vehicle to Infrastructure, V2P vehicle to pedestrian or V2V vehicle to vehicle.

The purpose of this thesis is to design innovative antennas solutions for the automotive market in order to allow the different V2X communications.

There are two main technologies that has been studied for this type of networks: the Wi-Fi based standard 802.11p and the so-called C-V2X based on the cellular network. The first one is a technology that is already available and some car maker are already implementing this solution on the cars. On the other hand, the C-V2X, nowadays based on the 4G or Long Term Evolution (LTE) standard but implemented with the 5G in the future, offers a more scalable technique. Starting from Release 14 and continuing with release 15 the 3GPP (Third Generation Partnership Project) [1] has defined the possibility for LTE devices to talk directly between them without passing through the network infrastructure, e.g. base stations. This improvement allows to reach very low communication latency that is necessary in case of V2X communications safety applications. An example for this type of application can be, in V2V communications, the transmission of an emergency brake information. Furthermore, this solution is based on an existing network that can be used to exchange long distance messages and does not need an expansive set up of a new infrastructures network. For these reasons it will be possible to see a large commercial distribution of V2X communications in parallel with the deployment of the 5G standard. Since these two technologies are strictly related, in this work we decided to investigate possible antennas solutions for the 5G in the automotive environment.

Figure 1.1 [2] illustrates a global snapshot of the allocated frequency band around

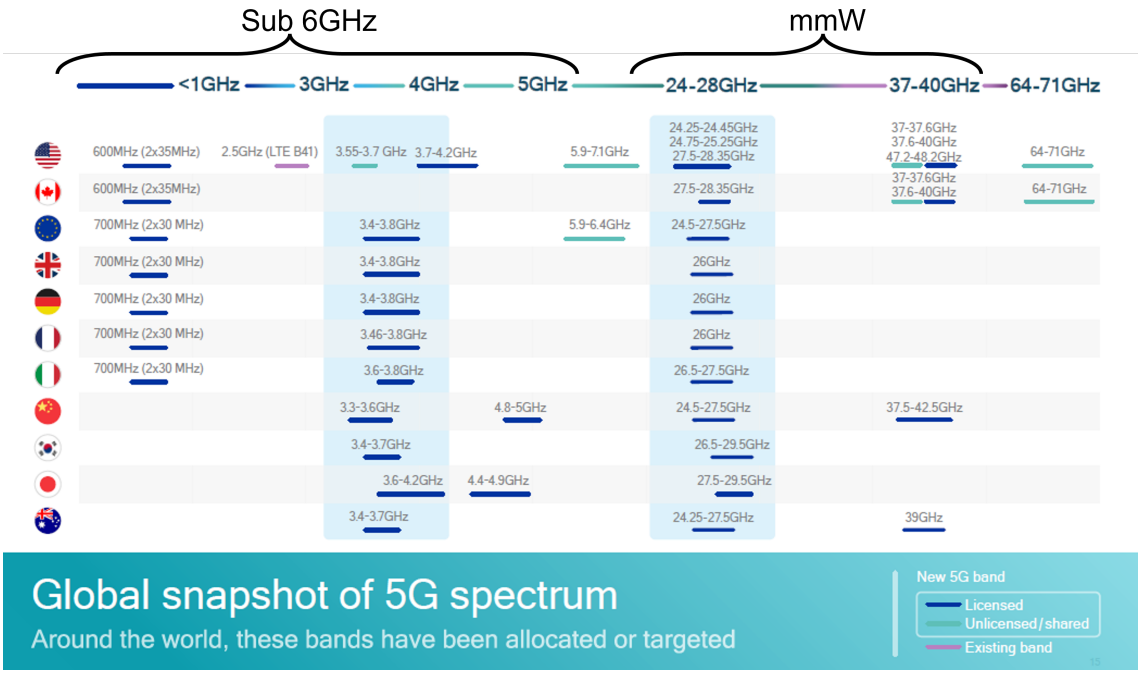

Figure 1.1. Global snapshot of allocated frequencies for 5G communications.

the world for the 5G communications. As it is highlighted in Fig.1.1 two main frequency regions can be grouped together. The first one can be considered an extension of the existing LTE standard, the so-called sub 6GHz band. An antenna designed for this band must cover all the LTE frequencies plus the new 5G extension, i.e. up to 5GHz. Furthermore, it has to operate also at 5.9GHz that is the allocated frequency that can be used only for V2X communications (both C-V2X and Wi-fi based standards).

The other main frequency band is located in the millimeter wave (mmW) region. In this region there is a lot of spectra available and the high requirement of bandwidth can be satisfied. For example, high bandwidth is required to allow Ultra Reliable Low Latency Communications (URLLC) and accomplish the continuously increasing throughput requirements. Unfortunately, in the automotive market the technology related to the mmW frequencies is not well known. For this reason, in order to gain know how about the mmW component and design procedure, the satellite communications (SatCom) field has been considered. For SatCom communications circular (or dual) polarization and wide scanning capability are a mandatory feature. These high performances requirements, in space applications, can be supported by a high cost and relatively bulky antenna. On the other hand, the automotive market has severe constraints in terms of costs and dimensions.

This work has been conducted in collaboration with ASK Industries S.p.A. an

automotive antenna supplier. All the information inserted in this thesis about the automotive market constraints and requirements comes out by their customers requests and the company experience.

This thesis is organized as follows: in Chapter 2 a 5G sub6GHz radiating element and a complete sub 6GHz automotive antenna module are described. Chapter 3 and Chapter 4 illustrate two SatCom mmW antennas. Finally, a possible mmW solution for the automotive market is provided in chapter 5. Conclusion follows.

Chapter 2

Automotive 5G Sub 6GHz Module

The so-called 5G sub-6GHz band extends the previous LTE standard to frequencies up to 5GHz. In this chapter a description of some possible implementation of a 5G sub 6GHz antenna for the automotive market are described. In addition, also the specific V2X frequency band allocated at 5.9GHz has been considered in the design.

First, the requirements and constrains of the automotive market are described. Then, a radiating element made by a folded tin sheet is presented. After that, a full 5G complete antenna module is designed considering commercial mechanical structure.

2.1 Requirements and constrains

As stated in the introduction, four different frequency bands can be identified to cover the worldwide allocated frequencies. This bands are: 0.6 GHz 0.96 GHz, 1.7 GHz - 2.7 GHz, 3.3 - 4.2 GHz and 4.4 GHz - 5 GHz. Furthermore, a dedicated band for vehicular communications has been allocated for this purpose at 5.9GHz. A 5G radiating element, should cover all this frequency bands with a good matching condition and with an acceptable radiation gain all around the vehicle. For the automotive industries, it is considered acceptable a return loss value $>$ 10dB (Voltage Standing Wave Ration (VSWR) $<$ 2) in the higher frequency bands (i.e. $>$ 1 GHz) [3]. On the other hand, a return loss $>$ 5dB (VSWR $<$ 3.5) is enough for the lower frequencies. For what is concerning the radiation characteristics of the antenna element, it is usually required an omnidirectional behaviour all around the vehicle. In the automotive market, the ”omnidirectionality” of the antenna is measured through a parameter called Linear Average Gain (LAG). The LAG is defined as the linear average of the antenna gain on given elevation cut [4]. Then, if a discrete number

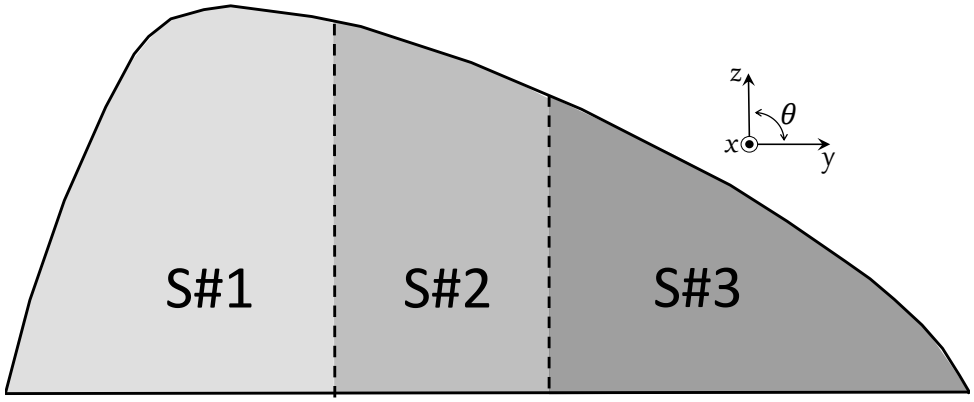

Figure 2.1. Sectional schematic view of a shark fin case. Three different sections of installation for the radiating elements are highlighted.

of measurement (N) is considered, the LAG is computed as

$$LAG(f,\theta) = 10log_{10}\left[\frac{\sum_{n=1}^{N} G_{linear}(f,\theta,\phi_i)}{N}\right] \tag{2.1}$$

where θ is the elevation cut and G_{linear} is the linear gain in the direction ϕ_i at the frequency f. For the frequency considered in the 5G sub6GHz (i.e. $<$ 6GHz) the free space attenuation is not very high. For this reason a LAG grater than -5dBi on the horizontal plane ($\theta = 0°$) is considered enough in the automotive market.

For low frequency bands, such as the one considered in the 5G sub6GHz, automotive commercial antennas are usually installed on the car roof top. This solution, allows to easily radiates in all the directions around the vehicle. In this placement, according to regulatory requirements, the antennas cannot be higher than 70mm in case of non-flexible elements [5]. Furthermore, aesthetic requirements has to be considered and the car manufacturer usually wants a low encumbrance and low cost antenna. The most used commercial radome for this type of antennas has a "shark-fin" shape [6], [7]. A sectional view of an example for this plastic case is illustrated in Fig.2.1. A sharkfin radome typically hosts more than one radiating element for different functions [8] e.g. Frequency Modulation (FM), Digital Audio Broadcasting (DAB), Global Navigation Satellite System (GNSS), mobile telephone. For the installation of these radiating elements the plastic case can be divided in three sections [9], [10] as it is shown in Fig. 2.1. Section S#1 is the tallest and usually hosts the Radio (FM, DAB) antenna or the main telephone antenna. Sections S#2 and S#3 are usually used for GNSS or other auxiliary antennas.

The correct exploitation of the low space available considering also the interaction with the other radiating elements is mandatory for a correct study of an automotive antenna. Lastly, also the robustness of the system has to be considered in the

design. In the next sections we show how all the requirements can be addressed for the correct realization of an automotive antenna.

2.2 Tin sheet secondary 5G antenna

In this section, 5G sub6GHz radiating element able to fit the space S#3 (see Fig. 2.1) of a sharkfin module is designed. Since the available space is limited, in order to reach the lower frequencies, i.e. make the electrical length of the radiating element as long as possible, a 3D metal design is exploited. In recent works [6], [8], radiating elements obtained through the folding of metal sheets are proposed to efficiently exploits the low space available. If the metal plate is sufficiently thick the radiating element is robust enough to be used in automotive environment. Furthermore, this type of technology allows to save costs (up to 50% [6]) respect to the commonly used Printed Circuit Board (PCB) fabrication technology [11], [12].

2.2.1 Design and simulations

The antenna has a monopole like structures with multiple branches that resonate at different frequencies. The longer branches are involved in the lower frequency radiation while the shorter ones are tuned to reach the desired matching in the whole frequency band.In particular, Tapered and stepped sections are exploited on the branches to increase the impedance matching. The feeding part has an elliptical shape to achieve a wideband behavior [12]. The structure is designed to fit in a commercial sharkfin module: the one produced for the AlfaRomeo Giulia. The simulated structure is illustrated in Fig. 2.2. It can be observed how the radiating element fits the sharkfin radome with a conformal shape.

Simulations [13] also include the cover that is made of plastic and modeled with dielectric parameters: $\varepsilon_r = 2.6$ and $tan\delta$ =0.01. Moreover, in order to takes into account the installation on the roof top, simulations are performed on a square ground plane with a 1m side. Simulation results in terms of matching and LAG are reported in Figs. 2.3(a) and (b) respectively. It is possible to observe that the results fulfil the previously listed requirements. The tuning on the radiating element has been conducted looking at the surface current distribution provided by the numerical simulator. In particular, looking at this parameter, it is possible to spot which part of the antenna is mostly involved in the radiation for a certain frequency. Thus, if a mismatch occurs for a certain frequency a change in the structure will be performed in the part where the surface currents have an higher density.

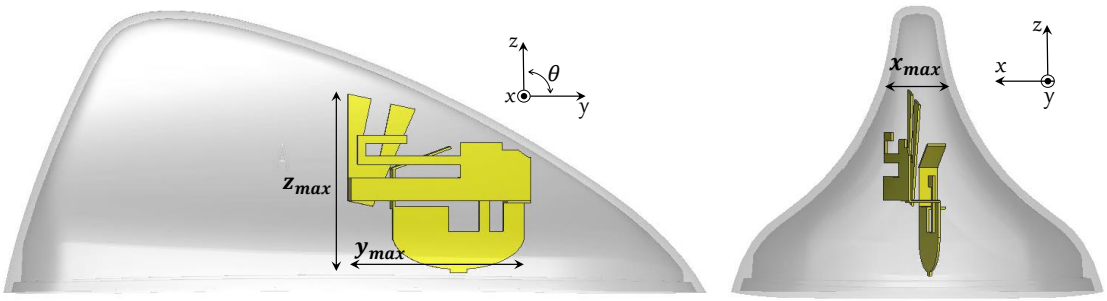

(a) **(b)**

Figure 2.2. Side view (a) and back view (b) of the designed 3D antenna inside the sharkfin radome. Maximum dimensions of the radiating element are: $z_{max} = 43mm$, $y_{max} = 44mm$ and $x_{max} = 15mm$.

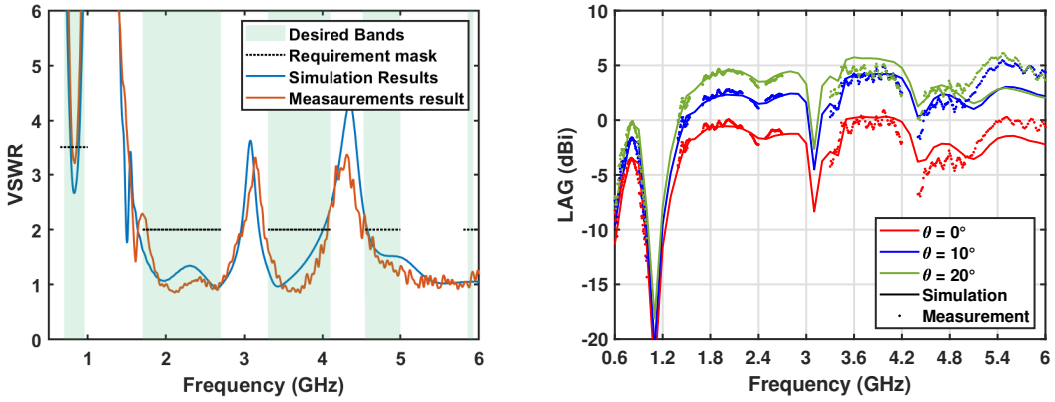

(a) **(b)**

Figure 2.3. (a) VSWR simulation and measurement results of the designed Radiating element. (b) Comparison between simulated and measured LAG results.

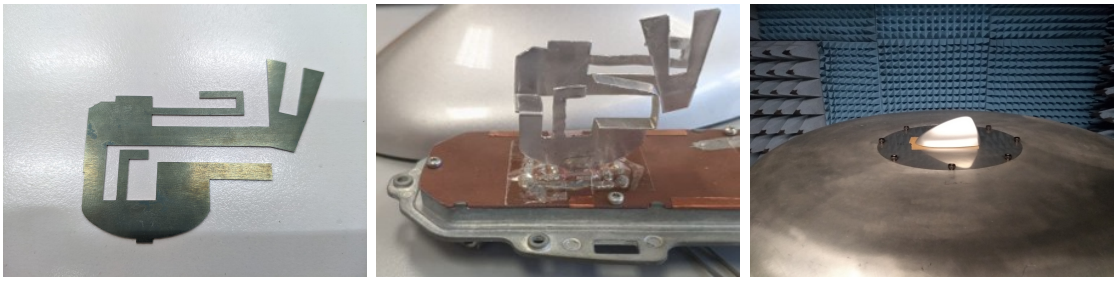

(a) **(b)** **(c)**

Figure 2.4. (a) Unfolded realized prototype. (b) Prototype folded and installed on the mechanical support. (c) Measurement setup of the prototype in the anechoic chamber.

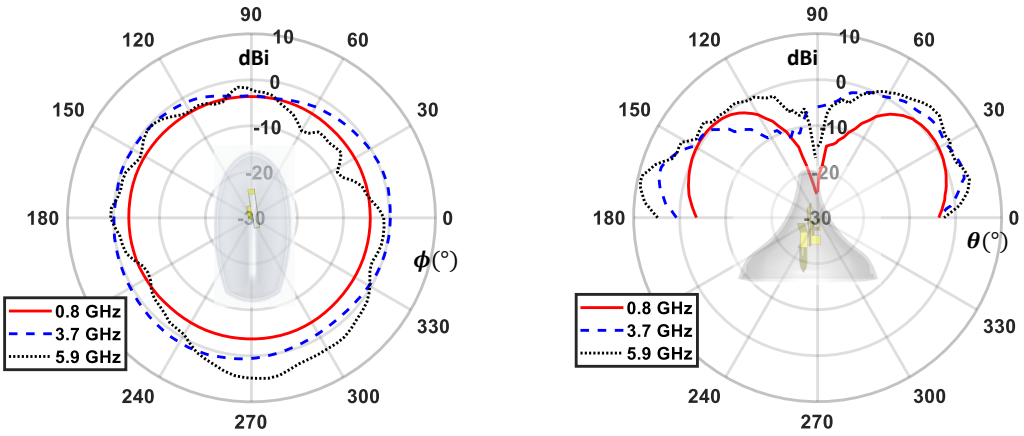

(a) (b)

Figure 2.5. (a) Radiation pattern measurement results on the $\theta = 0°$ cut for three different frequency. (b) Radiation pattern measurement results on the $\phi = 0°$ cut for three different frequency.

2.2.2 Prototype and experimental results

To keep the production costs as low as possible the proposed radiating element is designed to be feasible on a single metal sheet. In this way the antenna needs to be cut and folded only without any additional welding process. The prototype is realized through laser cut on a 0.5mm thick tin sheet. This metal thickness allows the radiating element to self sustain itself and be robust enough to the vibrations. Fig. 2.4(a) shows the unfolded metal sheet. The antenna is then folded and welded on an horizontal PCB placed in the sharkfin mechanics. A photograph of the final folded antenna prototype is illustrated in Fig. 2.4(b). The feeding is performed through a microstrip line in the bottom side of the horizontal PCB connected to a SMA connector (this type of connection will be described in details in Section 2.3).

Measurements are performed on the prototype installed on a circular ground plane with 1m diameter. A photograph of the measurement setup inside the anechoic chamber can be observed in Fig. 2.4(c). Measurements results, in comparison with the numerical simulations are reported in Fig. 2.3. It is possible to observe a very good agreement between experimental data and numerical data. In particular, alse the real prototype fulfil the requirements both in terms of matching and LAG. The omnidirectional radiation characteristics is confirmed from the radiation pattern plot in Fig. 2.5(a) where the measured pattern at $\theta = 0°$ plane is plotted for three different frequencies. Furthemore, in Fig. 2.5(b), where the $\phi = 0°$ cut is reported, it is possible to observe the monopole-like radiation behavior of the antenna. In fact, a zero-radiation occurs on the vertical direction. It can be also observed that,

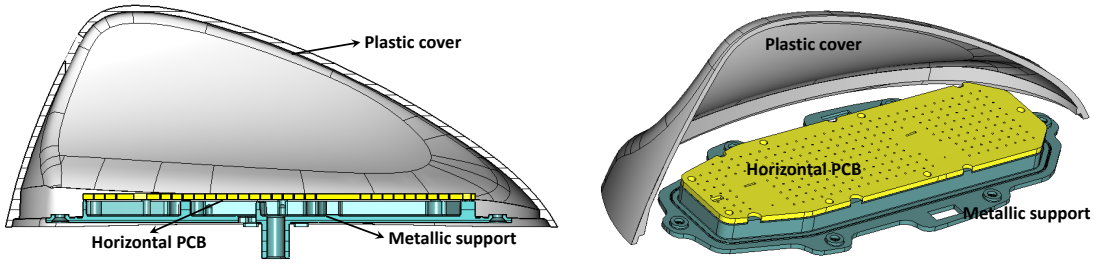

(a) (b)

Figure 2.6. Example of the sectional (a) and perspective (b) view of the mechanical structure of a sharkfin module.

differently from what it is expected from a monopole on an infinite ground plane, since the radiation element is positioned on a finite ground plane, the maximum value of the realized gain does not appear at $\theta = 0°$. From Fig. 2.5(b) it is clear that the maximum occurs between $\theta = 10°$ and $\theta = 30°$ depending on the operating frequency. In fact, for higher frequencies the metal plane appears bigger respect to the wavelength causing a more ideal ground plane behavior. LAGs measurement results for three different θ angles reported in Fig. 2.3(b) confirm this concept. In fact, in these curves the gain is higher respect to $\theta = 0°$ with a stronger difference at the lower frequencies.

2.3 5G complete antenna module

In the last section, a description of the design of a single radiating element is explained. In this section the design of a complete antenna module is addressed. In particular, inside the same sharkfin module three different element are placed. A 5G sub6 element, a V2X antenna and a Global Navigation Satellite System (GNSS) antenna. To accomplish the last requirements in terms of location precision the GNSS antenna needs to cover both the L1 (i.e. from 1559MHz to 1605MHz) and L2 (i.e. from 1190MHz to 1255MHz) bands. For this reason it is called GNSS High Precision (HP).

Figure 2.6 illustrates an example of the mechanical structure composing a sharkfin module. Excluding the radiating elements it is basically composed by three main components: the plastic cover, the horizontal PCB and a metallic support. The plastic cover, together with other plastic components are mainly used to provide water resistance to the module and accomplish aesthetic requirements. The horizontal PCB provides a support and electrical connection for the radiating elements. Furthermore on its layer facing the metallic support is often present some electronics

that compose the feeding network of the antenna. The horizontal PCB is electrically connected to the metallic support that provides an RF shielding for the electronic circuit. Furthermore, the metallic support is electrically connected to the car roof. The connection with the radiating element is usually performed in two different way, through a connector soldered to the horizontal PCB or through a "Pigtail" connection. The Pigtail connection consists on the soldering of a coaxial cable directly to the PCB. In this way it is possible to save costs and to have more degree of freedom regarding the feeding point position. In the designed module a Pigtail connection has been used.

The design of a complete antenna module can be performed with the following steps. Once the mechanics of the structure is defined, the radiating elements can me designed. First they will be considered alone on an infinite ground plane. After that they will be inserted inside the sharkfin mechanics and tuned if a mismatch occurs. Subsequently the horizontal PCB and the feeding network will be designed. All the previous action can be performed through numerical simulations. Finally, the prototype can be realized and if it necessary a last tuning can be performed directly on it.

2.3.1 Design and simulation

Radiating elements design

The 5G-sub6 radiating element is composed by a wideband monopole with two branches. The longer one is involved in the low frequency radiation while the shorter operates in the higher frequency region. This element is realized as a one layer PCB and installed vertically on the horizontal PCB. The substrate is FR4 with a thickness of 1.6mm. Since the V2X element needs to cover only a small portion of band around 5.9GHz a simple printed monopole has been used as a radiating element. Finally, the GNSS HP element is composed by a 4 pins commercial stacked patches with ceramic substrate. In particular, the smaller stacked element covers the L1 band while the larger patch radiates at the lower band L2. The complete module assembly in the simulation environment is reported in Fig. 2.7(a),(b) and (c) with the tow side views and the top view respectively.

The 5G-sub6 radiating element needs to be positioned where it can reach the higher dimension, in fact it is the element that needs to operate at the lower frequency. On the other hand, the stacked patch antenna is wide and need to be positioned where the plastic cover allows its placement. The positioning of these elements inside the module is then straightforward and depends on the mechanics.

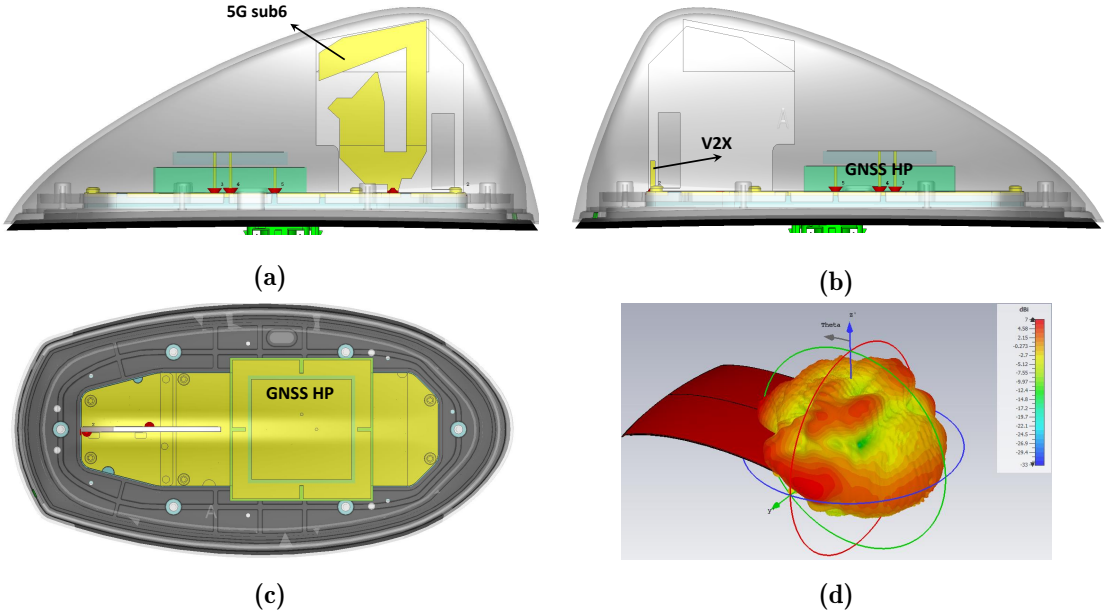

Figure 2.7. (a), (b) Side views of the complete antenna module. (c) Top view of the complete antenna module. (d) 3D radiation pattern simulation results of the V2X radiating element at 5.9GHz inside the sharkfin module placed on a real car roof top.

Due to its low encumbrance, for what is concerning the V2X monopole more degrees of freedom can be considered. For reasons regarding the radiation characteristics, the V2X antenna has been placed in the rear part of the sharkfin module as it can be notice in Fig. 2.7. This position makes the monopole radiates mainly toward the rear part of the vehicle. This behaviour can be observed in Fig. 2.7(d) where the 3D radiation pattern of the V2X element at 5.9GHz is reported. In this case, the radiation in direction of the back of the vehicle is preferable because of the curvature of the car roof. In fact, the roof is usually not completely flat and the sharkfin is placed in its rear part. The radiation toward the front can be then compromised and an auxiliary antenna is usually placed in the front of the vehicle to compensate this roof shielding effect. Since the V2X monopole is positioned next to the 5G-sub6 element the same PCB has been used in order to save costs. Furthermore, a hole in the substrate has been designed between the two antennas in order to reduce the coupling between them.

The simulation results of the 5G-sub6 element and the V2X monopole are reported in Fig. 2.8. In Fig. 2.8(a) is possible to observe that the requirements specified in Section 2.1 are accomplished except for a small portion of band in the lower frequency region of the 5G antenna. In this figure the S21 value between the two elements is also reported. It can be notice that thanks to the hole in the

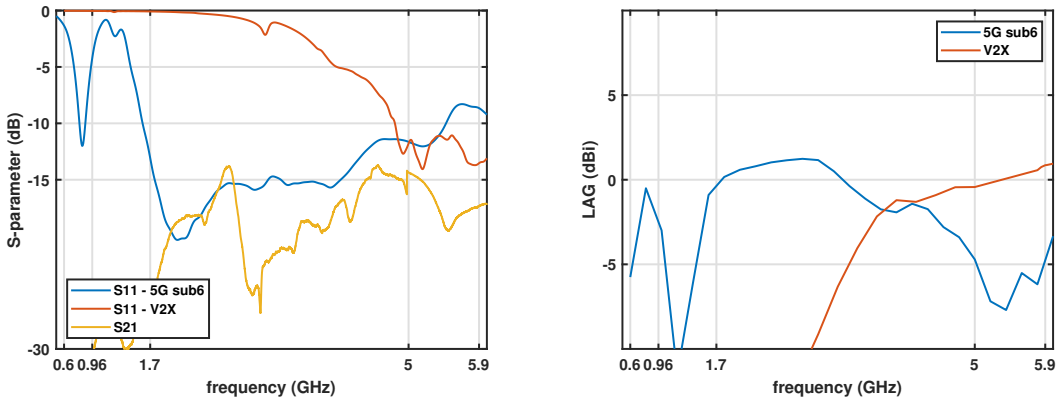

(a) **(b)**

Figure 2.8. (a) S-parameter simulation results for the 5G sub6 and V2X radiating elements. (b) LAG simulation results for the 5G sub6 and V2X elements.

vertical PCB substrate this parameter remains well below -15dB despite the small distance. In Fig. 2.8(b) the simulated LAG results are reported. Also in this case the requirements are fulfilled.

Feeding networks design

Two feeding networks need to be designed for this module. The first one is the hybrid coupler necessary to make the stacked patch radiates in Circular Polarization (CP). The second one is a matching network for the low frequency of the 5G-sub6 radiating element. The design has been performed through a commercial RF circuit simulator [14].

The selected commercial patch is a square patch that radiates in linear polarization. Each one of the stacked patches is fed through a pin exciting symmetrically the two linear polarization (E_x and E_y). To receive a GNSS signal, the Right Hand Circular Polarization (RHCP) is needed. From the literature [15] we know that CP is generated with two equal orthogonal E-field with a 90° phase shift between them. Since the selected patches can radiate two orthogonal linear polarization a feeding circuit able to shift them of 90° is necessary. The figure of merit that is used for evaluating the CP purity is the Axial Ratio (AR). The AR is computed as [16]:

$$AR = \frac{|E_x|^2 + |E_y|^2 + \sqrt{\gamma}}{|E_x|^2 + |E_y|^2 - \sqrt{\gamma}} \tag{2.2}$$

with γ:

$$\gamma = |E_x|^4 + |E_y|^4 + 2|E_x|^2|E_y|^2 cos[2(\angle E_x - \angle E_y)] \tag{2.3}$$

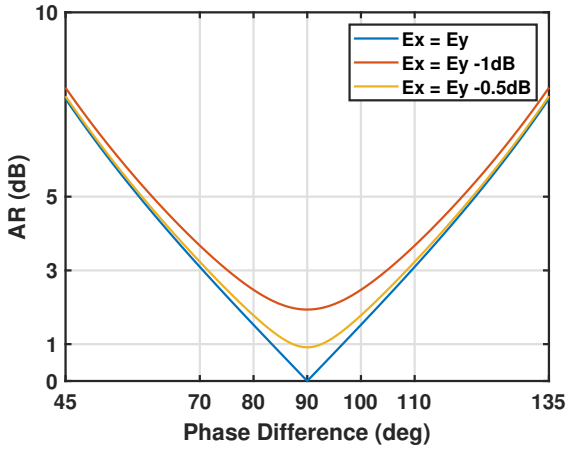

Figure 2.9. AR value versus the phase difference between the orthogonal E-field components E_x and E_y. Three difference between the magnitude of E_x and E_y are considered.

where E_x and E_y are the two orthogonal E-field components. According with Eqn. (2.2) the AR, if reported in dB, varies from 0 to $+\infty$. It is usually considered acceptable a value of AR $<$ 3dB. The relation between the magnitude and the phase of the orthogonal components (E_x and E_y) expressed with Eqn.s (2.2) and (2.3) is reported in Fig. 2.9. This figure highlights how the correct design of the hybrid impacts on the performance of the GNSS.

To achieve the desired phase shift between the patch pins, a lumped element 90° hybrid is designed for the two frequency bands. The circuit schematic is reported in Fig. 2.10(a) while the component values are listed in Tab. 2.1. The designed 90° hybrid is composed by two LC cells closed on a 50Ω resistor. The circuit should cause a +90° shift of the signal at the port "Patch Pin 1" respect to the signal at the port "Patch Pin 2". A bypass capacitor (C5) is inserted in series to the common port. In addition to the desired phase shift the circuit should equally split the power between the pins of the patch. Simulation results of the designed circuit are reported in Fig. 2.11. The results are obtained imposing at the pin patches port the impedance provided by the vendor. In particular from Fig. 2.11(a) and Fig.2.11(b) can be observed the phase difference and the amplitude difference between the pins in the desired L1 and L2 frequency bands. The obtained phase difference remains in the range $90° \pm 5°$ while the magnitude difference remains in the range $0dB \pm 0.5dB$. Furthermore in Fig. 2.11(c) and (d) the S- parameters results from the common port are reported. The designed hybrid circuit has a good matching ($<$ -20dB) and equally splits the power between the pin patches ports (S21 $\approx -3dB$).

The matching network for the 5G-sub6 element is used to increment its matching in the low frequency band. The schematic can be observed in Fig. 2.10(b) while

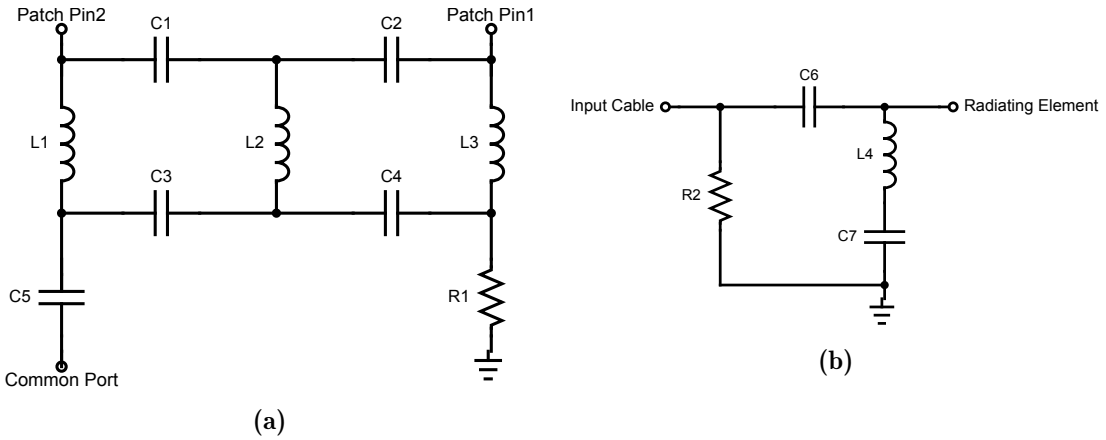

Figure 2.10. (a) Schematic of the 90° hybrid for the GNSS patch. (b) Schematic for the matching network for the 5G-sub6 element. Component values are listed in Tab. 2.1.

Label	Radiating element	Value
C1, C2, C3, C4	L1 patch	2.2pF
L1,L2,L3		4.7nH
C5		100pF
R1		50Ω
C1, C2, C3, C4	L2 patch	2.7pF
L1,L2,L3		6.8nH
C5		100pF
R1		50Ω
C6	5G-sub6	8.2pF
C7		5.6pF
L4		20nH
R2		10kΩ

Table 2.1. Components value of the two designed feeding networks reported in Fig. 2.10.

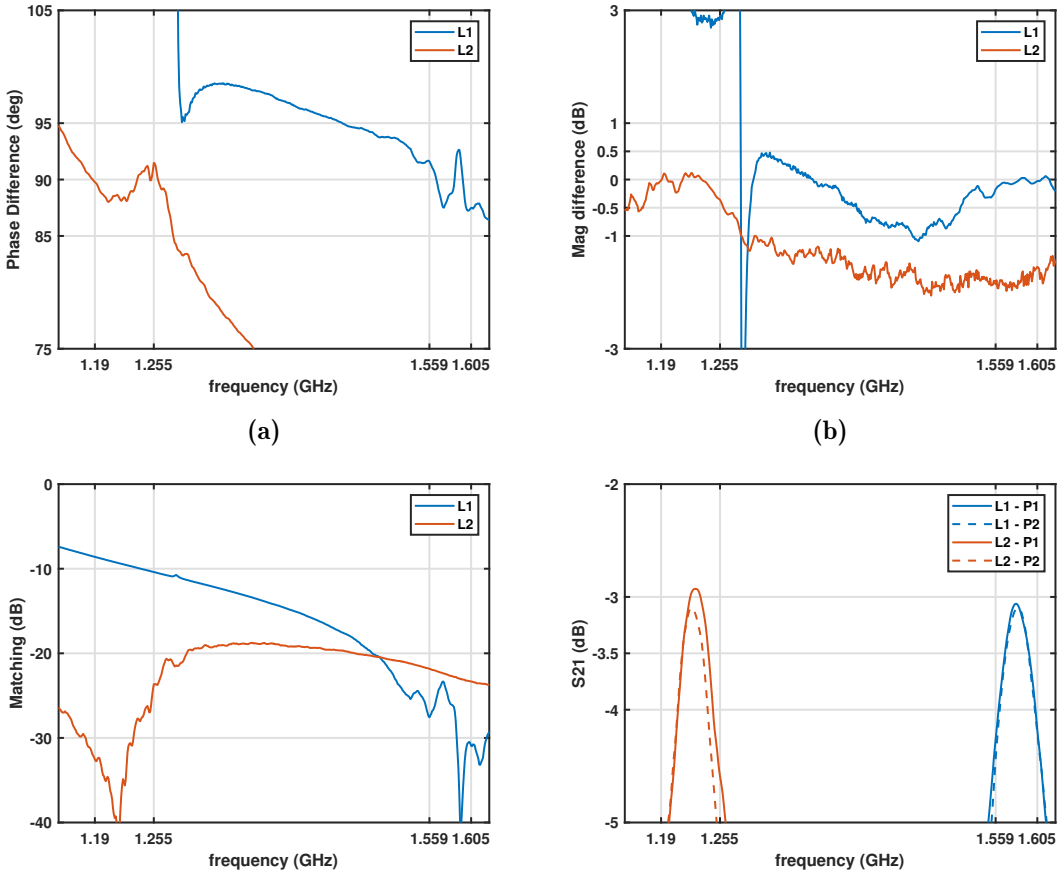

Figure 2.11. Simulation results of the hybrid circuit illustrated in Fig.2.10(a). (a) Phase difference between the two patch pins. (b) Amplitude difference between the two patch pins. (c) Matching obtained from the common port. (d) Transmission parameter between the patch pins ports and the common port.

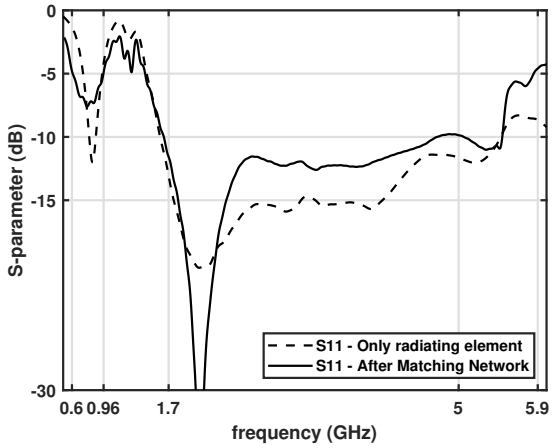

Figure 2.12. Input matching of the 5G-sub6 radiating element with and without matching network.

the components value are listed in Tab. 2.1. The circuit is composed by a series capacitor and a parallel LC resonant circuit. An high value resistor is connected between the Pigtail and ground for production reasons. For the analysis of the circuit the previously simulated radiating element input impedance has been used. In Fig. 2.12 the comparison between the 5G-sub6 radiating element matching is reported.

2.3.2 Prototype and experimental results

After the design performed through simulations the prototype of the module has been realized. In Fig. 2.13(a), (b) and (c) it is possible to observe the side views and top view of the prototype. Furthermore, a picture of the horizontal PCB is reported in Fig. 2.13(d). In this image in is possible to observe the lumped element circuit composing the hybrid couplers, a Pigtail pad and the hole for the vertical PCB installation. On the Pigtail pad the incoming coaxial cable will be soldered to feed the antenna elements. In particular, the inner conductor is soldered on the square pad connected to the circuit while its metallic shield is soldered to the ground-connected pad.

As it is described in Sec. 2.2.2 the antenna measurements has been performed with the antenna module installed on a circular ground plan with 1m of diameter. This allows to take in consideration the roof top without using a real car. A picture of the measurement setup can be observed in Fig. 2.4(c). In Fig. 2.14 a comparison between the measured and the simulated S11 is reported. Here can be observed that both the 5G-sub6 element and the V2X element fulfil the requirements with a good

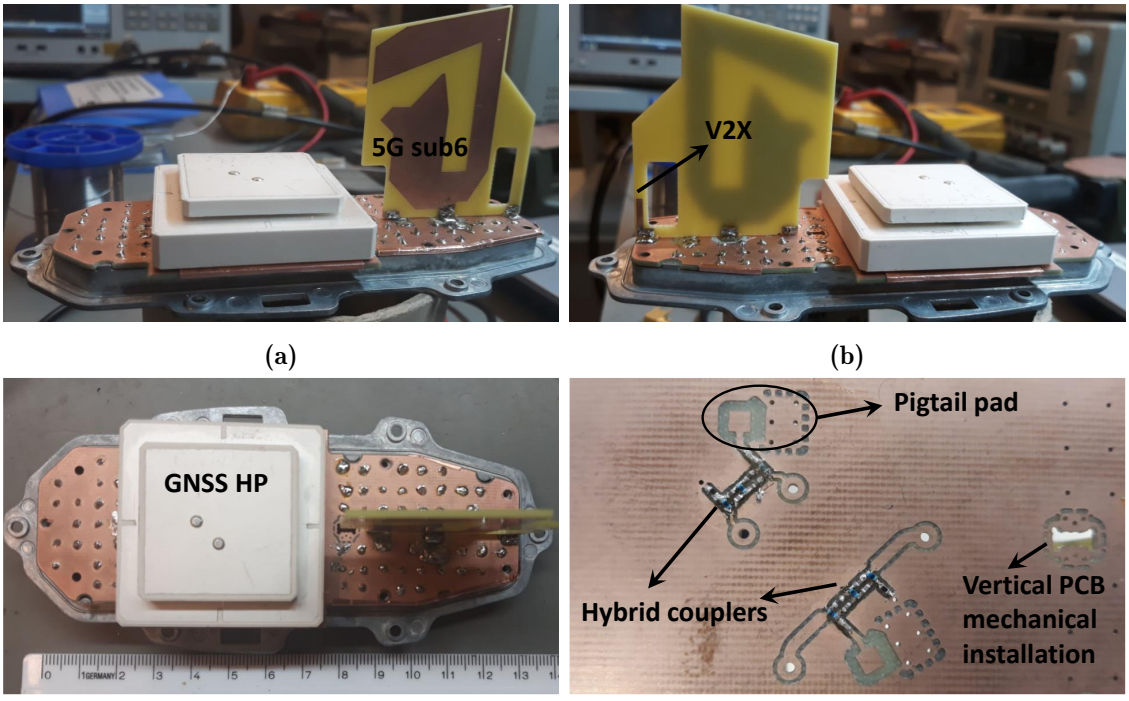

Figure 2.13. (a), (b) Side views of the complete antenna module prototype. (c) Top view of the complete antenna module prototype. (d) Detail of the circuit face of the horizontal PCB.

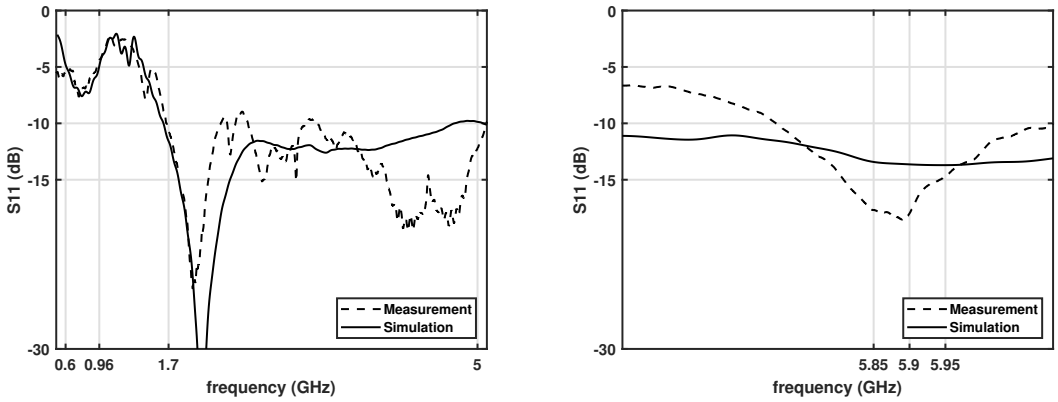

Figure 2.14. (a) Matching comparison between simulation and measurement results for the 5G-sub6 element. (b) Matching comparison between simulation and measurement results for the V2X element.

agreement between numerical and experimental results.

The experimental results regarding the radiation characteristics in terms of LAG are illustrated in Fig. 2.15. Also in this case the the matching between measurements and simulations is good and the requirements are satisfied also for both the elements. Also in this case it is possible to observe the finite ground plane behaviour previously described in Sec. 2.2.2. For the V2X element is reported also the radiation pattern on the $\theta = 0°$ cut. This result can be observed in Fig. 2.16(a). In the figure can be noticed that radiation is mainly directed toward the rear part of the module. This behaviour accomplish to the radiation requirement for the V2X element previously described.

Finally, the radiation characteristics of the GNSS HP can be analyzed. In Fig. 2.16(b) the measured AR for the bands L1 and L2 in the vertical direction ($\theta = 0°$) are reported. The measurements shows good results (AR $<$ 3dB) for both the frequency bands. In Fig. 2.17 the radiation pattern in RHCP on the side view ($\phi = 90°$) and on the back view ($\phi = 0°$) of the GNSS HP are shown. The results show the typical shape of a patch antenna radiation pattern with a ripple deformation on it. This perturbation on the patterns is mainly caused by two factors. The first one is the plastic cover of the antenna module that is not uniformly distributed on the patch antenna. The second one is the non-negligible step between the horizontal PCB and the ground plane. However, since the gain of the antenna remains almost everywhere grater than 0dBi in the range $30° < \theta < 150°$, this effect can be consider not strongly affect the GNSS performances.

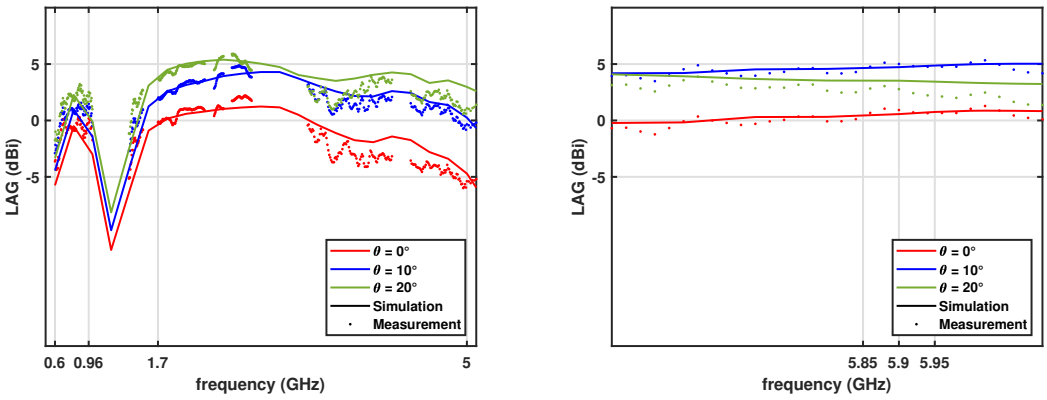

(a) (b)

Figure 2.15. (a) LAG comparison between simulation and measurement results for the 5G-sub6 element. (b) LAG comparison between simulation and measurement results for the V2X element.

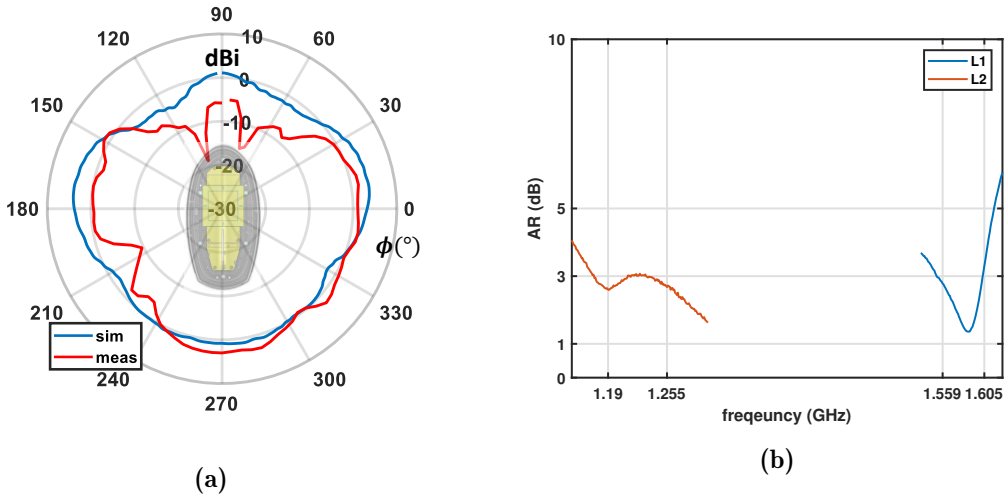

(a) (b)

Figure 2.16. (a) Comparison between simulation and measurements of the radiation pattern on the cutting plane $\theta = 0°$ for the V2X element. (b) AR measurement results in the vertical direction ($\theta = 90°$) for the GNSS HP.

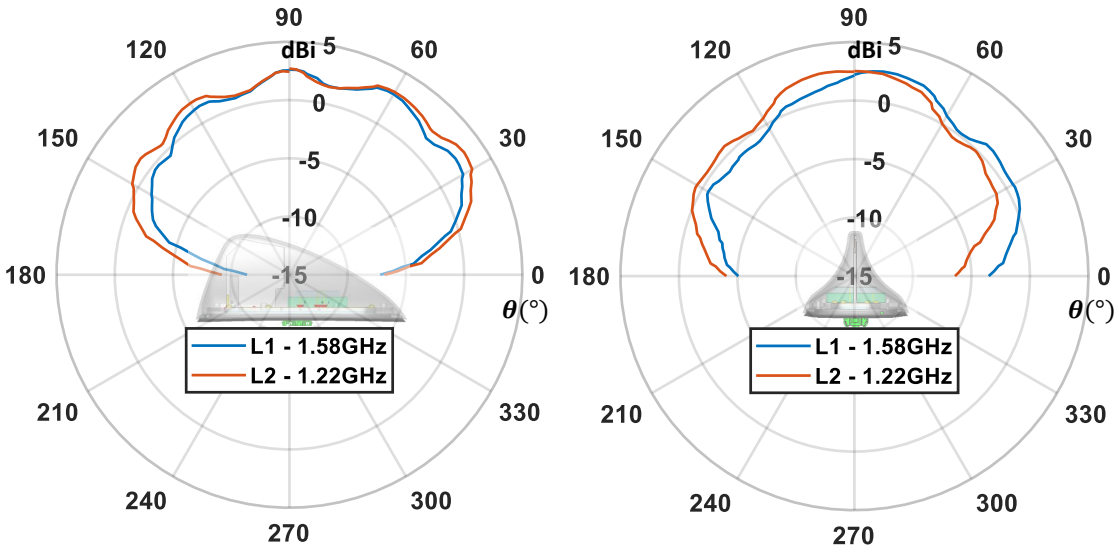

(a) **(b)**

Figure 2.17. (a) RHCP radiation pattern measurement results for the GNSS HP on the cutting plane $\phi = 90°$. (b) RHCP radiation pattern measurement results for the GNSS HP on the cutting plane $\phi = 0°$.

2.4 Conclusions

In this chapter automotive antennas for the 5G-sub6 connectivity are analyzed. In particular the requirements and the constrains of a roof top antenna are illustrated. Then, a novel 3D radiating element is presented and finally a complete sharkfin module design is described. In the next two chapters we are going through the design of antennas for space applications. In fact, before moving to the 5G mmW frequency range for the automotive market, the space case of study has been considered. In this field of applications the mmW frequency band is well established technology and its study can provide important knowledge about its development in a different market.

Chapter 3

Antenna for space applications: Multimode pillbox beamformer

In space application antennas or more specifically satellite communications (SatCom) the mmW frequency band is used since years. For this reason a study on space market antennas is performed. This allows to bring the know how acquired on this field to the automotive market. In this chapter and in chapter 4 two novel structure working in the mmW frequency region for SatCom are presented. These works were realized in collaboration with IETR (Institut d'Electronique et des Technologies du numéRique) of Rennes (FR).

This chapter present the design of a multimode pillbox beamformer in the Ka band (27.5-31GHz) that is the SatCom transmission band. After a brief introduction on this type of beamformers the exploited coupling mechanism is explained. Then, a description of the quasi optical system is provided. Finally, an antenna that exploits the designed system is proposed.

3.1 Pillbox Beamformer

In SatCom applications, antennas with high gain and wide angle scanning capability are required. In fact, this two characteristics together with a double polarization capability is mandatory to increase the SatCom link robustness [17] [18]. Antenna beam scanning and high gain it is usually obtained through the exploitation of phased arrays [15]. In phased array systems the main beam can be tilted by changing the phase of the signal that feeds the single elements of the array. This phase can be changed by the means of the so-called beamforming networks (BFNs). Among them the most promising BFNs in terms of cost and dimensions are the one based

on quasi-optical system. Examples of this type of BFNs can be the Rotman lens [19] the Luneburg lens [20], and the pillbox beamformer. These quasi-optical systems generates a 2D illumination that can be used to feed the most recent developed radiating system such as Leaky wave antennas (LWAs) [21], metasurfaces antennas [22] or Continuous Transverse Stub (CTS) arrays [23].

Pillbox beamformers are composed by two stacked Parallel Plate Waveguides (PPWs) coupled by a parabolic reflector as shown in 3.1. In particular, feeds located in the focal plane of the parabolic reflector launch a cylindrical wave in the bottom PPW (or feed layer PPW). Coupling slots/apertures in the middle metallic layer transfer and phase the launched wave to the second PPW. In general, such beamformers present a single mode operation either Transverse Electro-Magnetic (TEM) [21] [24] or first Transverse Electric (TE_1) [25]. The structure presented in 3.1 is the first example in the open literature operating as a dual-mode quasi-optical beam former. The exploited TEM and TE_1 modes presents an orthogonal E-field distribution [26]. Thanks to that this structure can be used to feed directly dual linar polarization antennas [27][28] or circularly polarized antennas [29]. Two different paths of propagation are exploited for the TEM and TE_1 modes to separate the coupling mechanisms and provide a degree of freedom for the optics associated to the two modes. The two paths are illustrated in Fig. 3.2 for the unit cell highlighted in Fig. 3.1 behind the design of the quasi-optical system.

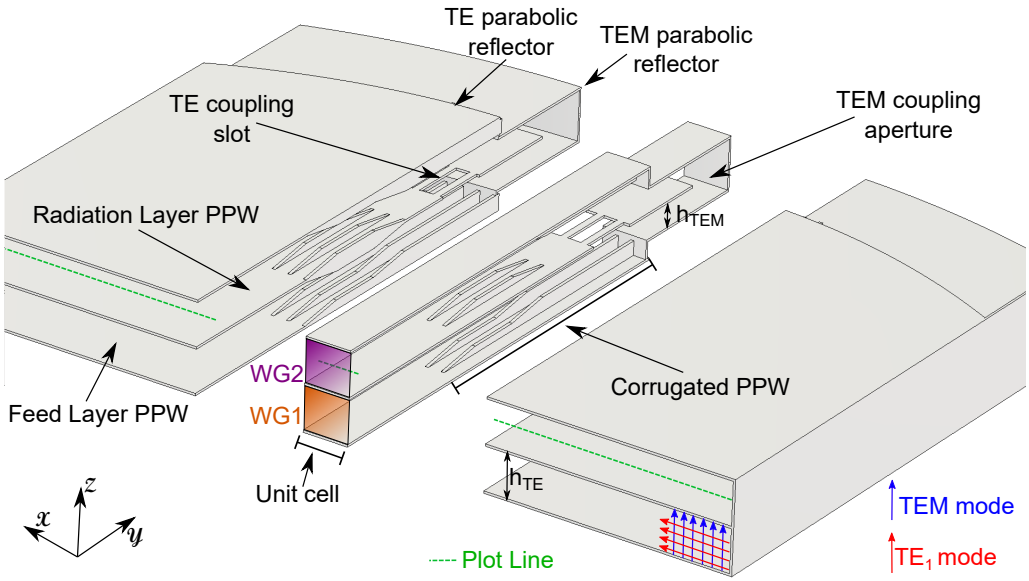

Figure 3.1. Perspective view of the dual mode pillbox beamformer.

3.2 Structure and Coupling Mechanism

As stated in [21] and [25], a pillbox beamformer and in general quasi-optical beamformers can be analyzed as directional couplers by using a representative unit cell. Such a unit cell is generally assumed around the vertex of the parabolic reflector to consider normal incidence of the incoming mode and to approximate the reflector as planar as shown in Fig. 3.1. In the shown quasi-optical system, the two PPWs operate in a multi-mode frequency region i.e. $h_{TE} > \lambda_{max}/2$ where λ_{max} is the wavelength associated to the lowest operating frequency. In this working region the only three propagating modes in the PPWs are the TEM, the TE_1 and the first Transverse Magnetic (TM_1). In particular, TE_1 and TEM modes present orthogonal E-field components as sketched in Fig. 3.1. On the other hand, the TM_1 mode present an E-field component along the z-axis as the TEM one. For this reason, these two modes can easily couple with an impact on the field profile of the TEM mode. Such a coupling should be then avoided.

The proposed pillbox system and corresponding unit cell can be derived in three different parts as it is shown in Fig. 3.1 and Fig. 3.2: 1) corrugated PPW; 2) TE coupler; 3) TEM coupler. These building parts will be described in the following.

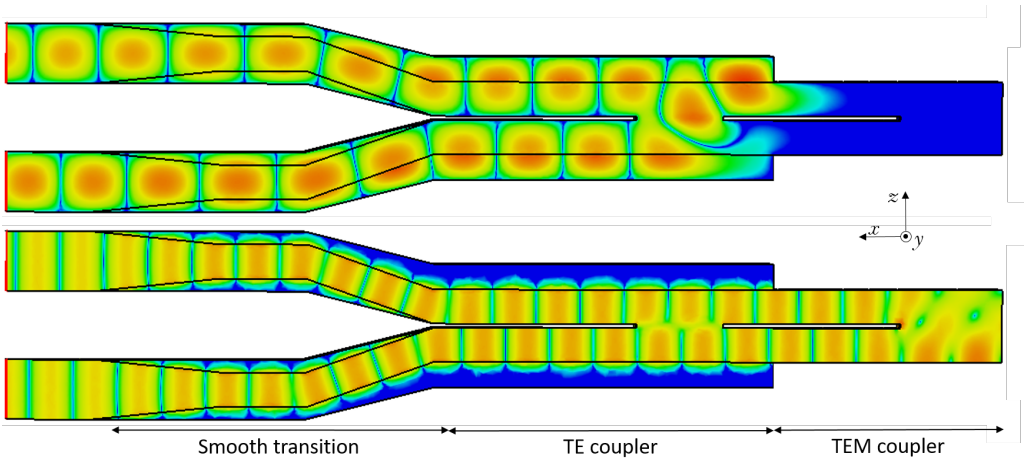

Figure 3.2. E-field profiles for the TE_1 and TEM modes within the unit cell.

Corrugated PPWs are composed by a periodic arrangement of rectangular ridges located on each plate of the guiding structure. The geometrical features of the unit cell of the corrugated PPW are shown in Fig. 3.4(a)-(b). As long as the following three conditions are satisfied only TEM and TE_1 modes can propagate: the periodicity of the ridges (p_{cor}) is electrically small respect to λ_{max}; $h_{TEM} < \lambda_{max}/2; \lambda_{max} < h_{TE} < \lambda_{min}$, where λ_{max} and λ_{min} are the wavelength at the lower and the highest frequency of operation, respectively. The dispersion diagram of the

corrugated PPW is provide in Fig. 3.4(c). The TM_1 is in cut-off until 40.3 GHz. For matching, a tapering transition in introduced at the end of the corrugation. Note that the TEM is mainly confined between the corrugations of the PPW while the TE_1 propagates in the full structure, as clearly seen from Fig. 3.1.

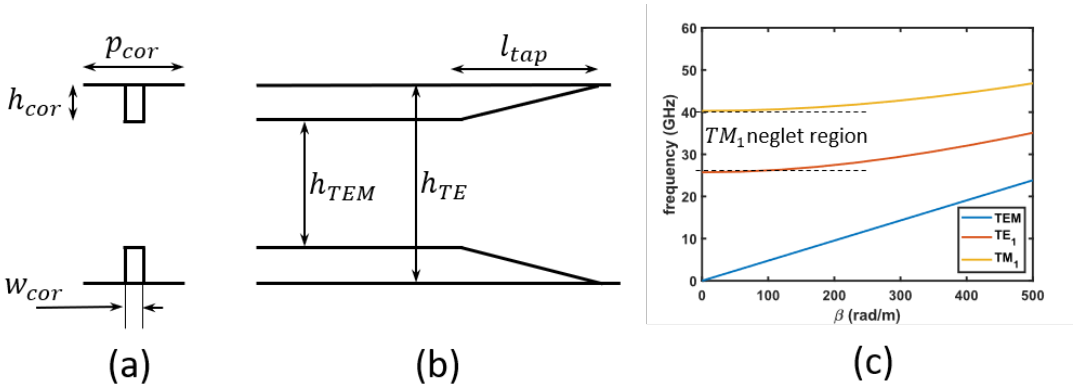

Figure 3.3. Corrugated PPW (double sided). (a) Front view; (b) Side view with smooth transition; (c) Dispersion diagram. Dimensions are reported in Tab. 3.1.

In some parts of the quasi-optical beam former a single sided corrugated PPW is adopted to ease the design. Such a structure, geometrical features and dispersion diagram are shown in Figure 4. In this case, The TM1 is in cut-off until 41.5 GHz.

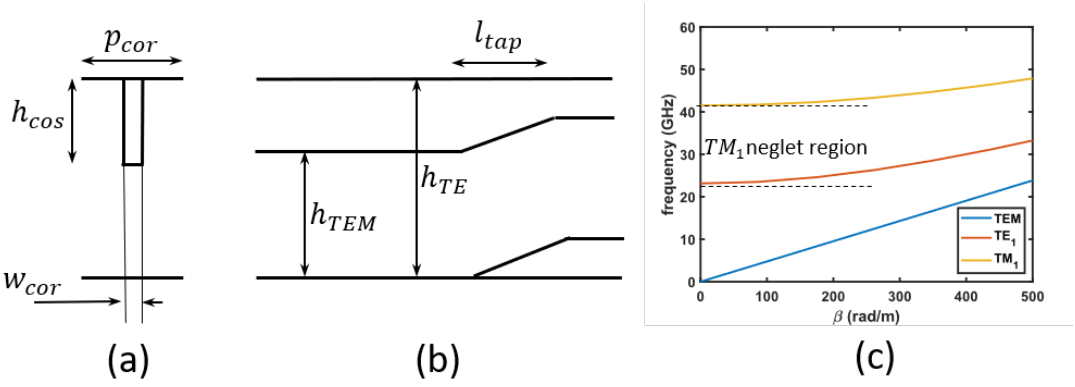

Figure 3.4. Corrugated PPW (single sided). (a) Front view; (b) Side view with smooth transition; (c) Dispersion diagram. Dimensions are reported in Tab. 3.1.

The TE_1 coupler consists in of a slot aligned along the axis of the parabolic reflector as shown in Fig. 3.1. The reflecting wall of the coupler is achieved by reducing the height of the PPW to $h_{TEM} < \lambda_{min}/2$ right after the coupling slot, placing the TE_1 mode in cut-off.Figure 3.5 provides the top view of the coupler.

The simulation setup is composed by the unit cell with periodic boundaries conditions on the two lateral sides. Two waveguide ports are placed at the feed

(bottom PPW) and radiation side (top PPW) to derive the scattering matrix and operating modes. The simulation results for the S-matrix are shown in Fig. 3.6(b) for a unit cell with geometrical sizes as in Fig. 3.5 . The TE_1 coupler is matched in the band 26-32 GHz, while the coupling with the other modes is avoided, i.e. $S21_{TEM,TE}$ and $S21_{TM,TE}$ < -50 dB.

The TEM coupler is composed by an aperture (ls_{TEM} in Fig. 3.5) contouring the parabolic reflector profile. This coupler is realized between two mono-modal PPWs as in a classical pillbox beamformers [21]. In such configuration the TE_1 and TM_1 modes are in cut-off. The simulation results for the S-matrix are shown in Fig. 3.6(a). Also in this case, the coupler is well matched in the band 26.5-32 GHz and the coupling with the other modes is very low. It is worth mentioning that the length of the mono-modal PPW (lp_{TEM} in Fig. 3.5) does not affect the results. This parameter is key to modify the focal length of the TEM quasi-optical system without affecting the results and the TE_1 optics.

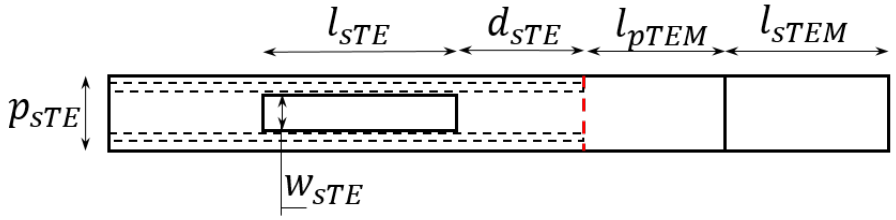

Figure 3.5. Top view of the TE1 coupler. Black dashed lines represent the corrugations profile while the red dashed line represents the TE parabolic reflector. Dimensions are reported in Tab. 3.1.

3.3 Quasi Optical System

The quasi-optical system can be schematically summarize as described in Fig. 3.7. The input horn is placed along the focal line of the two parabolic reflectors. These have two different curvature in order to keep their focal lengths in the same position. The input horn launches a cylindrical wave in the lower PPW (feed layer in Fig. 3.1). If it is in the focal position, the parabolas reflect the wave coupling a quasi plane wave in the upper PPW (radiation layer). When the horn is shifted from the parabola axis (S_h), the direction of propagation of the plane wave is tilted. The direction of propagation of the wave in the radiation layer PPW will change the scan angle of the antenna beam. The wave tilting can be approximately computed

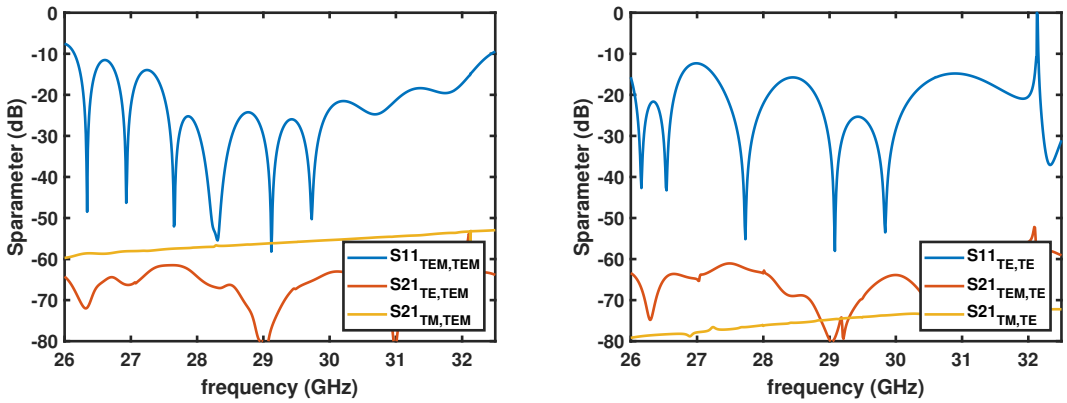

(a) (b)

Figure 3.6. Scattering parameters for the unit cell of the (a) TEM and (b) TE_1 coupler.

label	description	dimension (mm)
w_{cor}	corrugation width	0.5
h_{corr}	two-side corrugation height	1.5
p_{corr}	corrugation periodicity	1.5
h_{TEM}	single mode PPW height	4
h_{TE}	multimode PPW height	7
l_{tap}	tapering length	10
h_{cos}	one-side corrugation height	3
p_{sTE}	unit-cell periodicity	3
l_{sTE}	TE coupling slot length	10.5
w_{sTE}	TE coupling slot width	2.1
d_{sTE}	distance between the TE slot and reflector	5.5
l_{pTEM}	length of the single mode PPW	55
l_{sTEM}	length of the TEM coupling slot	12

Table 3.1. Dimensions of the multimode pillbox system. Labels refer to the dimensions reported in the figures 3.3, 3.4 and 3.5.

as [30]

$$\varphi \approx \frac{S_h}{F} \cdot \frac{\beta}{k_0\sqrt{\varepsilon_r}} \tag{3.1}$$

where S_h is the horn displacement on the focal line respect to the parabola axis, F is the focal length of the parabolic reflector, k_0 is the wave number in the free space, ε_r is the relative permittivity of the medium and β is the propagation constant of the mode. Since [26]

$$\beta_{TEM} = k_0\sqrt{\varepsilon_r}, \tag{3.2}$$

the TEM mode shift can be computed as

$$\varphi_{TEM} \approx \frac{S_h}{F_{TEM}} \tag{3.3}$$

where F_{TEM} is the focal length of the TEM reflector. On the other hand, β_{TE_1} is [26]

$$\beta_{TE_1} = \sqrt{k_0^2 - \frac{\pi}{h_{TE}}^2}, \tag{3.4}$$

thus, the TE_1 shift can be computed as

$$\varphi_{TE_1} \approx \frac{S_h}{F_{TE}} \cdot \frac{\beta_{TE_1}}{k_0\sqrt{\varepsilon_r}} \tag{3.5}$$

where F_{TE} is the focal length of the TE parabolic reflector. Equation (3.5) shows that the TE_1 shift (φ_{TE_1}) is frequency dependent. As stated in section 3.2, the distance between the two reflectors can be changed without affecting the coupling mechanism. In particular, this feature can be achieved by changing the length of the monomodal PPW part (l_{pTEM} in Fig. 3.5). Equations (3.3) and (3.5) have been used to select the proper value of F_{TEM} to have the same wave tilting for the two modes at the center frequency of the Ka band i.e. 29.25GHz. F_{TE} has been chosen almost equal to $10 \cdot \lambda_{gTE_1} = 2\pi/\beta_{TE_1} = 155$mm. Thus, F_{TEM} results equal to 225mm. Fig. 3.8 illustrates the scan angle for the two modes for three different horn displacement. The results obtained with full wave simulations are in good agreement with the previously described approximated formulas.

To verify the correct operation of the pillbox beamformer the phase of the electric field of the the quasi-plane wave is studied. This is a very important parameter since the E-field in the upper PPW feeds the radiating part. A plot line (PL) is drawn along the direction orthogonal to the propagation one (green dotted line in Fig. 3.1). The considered plot line is long as the -10dB tapering of the electric field. For clarity it is considered the taper length of the TE_1 mode which is lower than the TEM one (see section 3.4.1). The E-field phase along the line should be constant when

there is no feed horn shift (i.e. $S_h = 0$). When a shift occurs the phase (ph) can be computed as

$$ph = k_0\sqrt{\varepsilon_r}sin(\varphi)pos_{PL} \tag{3.6}$$

where φ is the shift for TEM and TE_1 computed with Equations (3.3) and (3.5) respectively and pos_{PL} is the position along the plot line. In Fig. 3.9 are reported the full wave simulation results for 4 different feed horn positions. For broadside direction the maximum phase variation is 20° for TEM mode and 40° TE_1. For the other positions the simulations results are compared with the phase obtained from Eqn. (3.6). Also in these cases the results are satisfactory with a good agreement between simulations and numerical analysis.

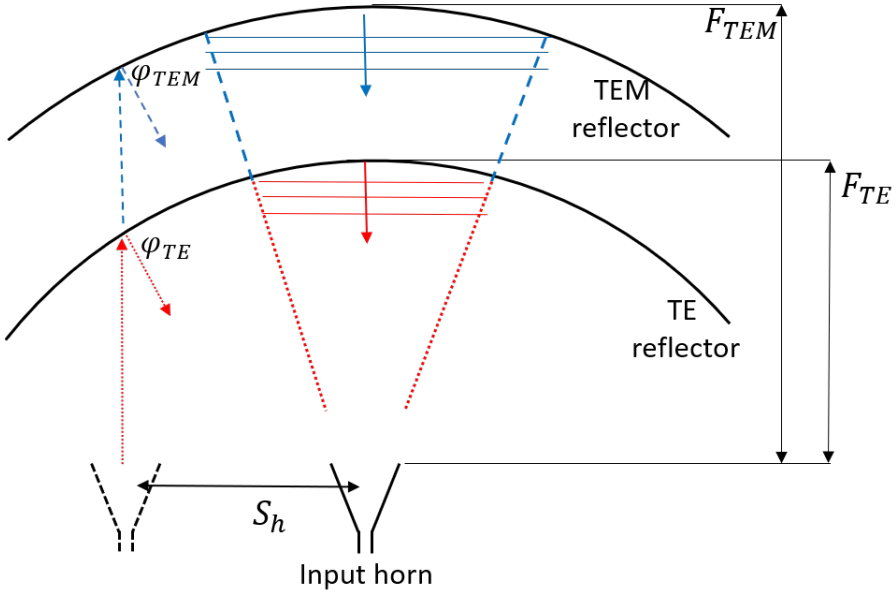

Figure 3.7. Schematic representation of the quasi-optical system. Red dotted lines and blue dashed lines represent the TE_1 and TEM modes, respectively.

3.4 Validation Antenna

In this section a possible antenna comprising the proposed pillbox beamformer is presented. The antenna is composed by, an input horn, the previously described pillbox system and a radiating tapered aperture. The structure is validated through full wave simulations. In particular a full metal antenna is here proposed. The overall antenna structure is illustrate in Fig. 3.10. The overall antenna dimensions are w_{tot} = 300mm, l_{tot} = 230mm and h_{tot} = 65mm. In order to design an antenna that

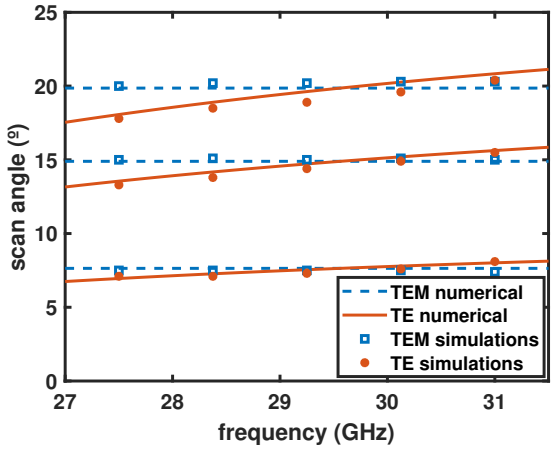

Figure 3.8. Scan angle versus frequency for the TE_1 (orange solid lines) and TEM (blue dashed lines) mode. The results obtained through full-wave simulations are represented by blue squares for TEM mode and orange dots for the TE_1 mode. The results refer to a horn displacement (S_h) of 30, 60 and 80 mm in the focal plane of the parabolic reflector.

can be realized, the tolerances and the feasible minimum dimensions are considered referring to previously published works [24][27][28]. As stated before the antenna is designed to have optimal working condition in the SatCom transmission band i.e. from 27.5GHz to 31GHz.

3.4.1 Input horn

In the designed antenna, the cylindrical wave is launched in the feed PPW through an horn antenna. Two different input horns have been designed, one for each polarization. In order to allows the connection with commercial devices the horns are designed with dimensions that allows the feed through a standard WR28 rectangular waveguide. Nonetheless, the same aperture, length and height has been used for both the horns. In Fig. 3.11 (a) the structure and the dimensions of the two horns are showed.

Fig. 3.11 (b) shows the radiation patterns of the input horns inside the feed PPW. The results highlight that the radiation characteristic for the two modes is very similar. In particular, if the -10dB tapering angle is considered, it is $\Delta\Phi_{TEM,TE} \approx \pm 25°$. Even if the horn aperture is the same for the two modes, the distance between the reflectors will cause a different illumination of the parabola. Consequently the -10dB amplitude tapering of the coupled quasi plane wave has a different length for the two modes. The -10dB tapering for TEM and TE_1 can be computed as

$$l_{-10dB} = 2 \cdot F sin(\Delta\Phi), \tag{3.7}$$

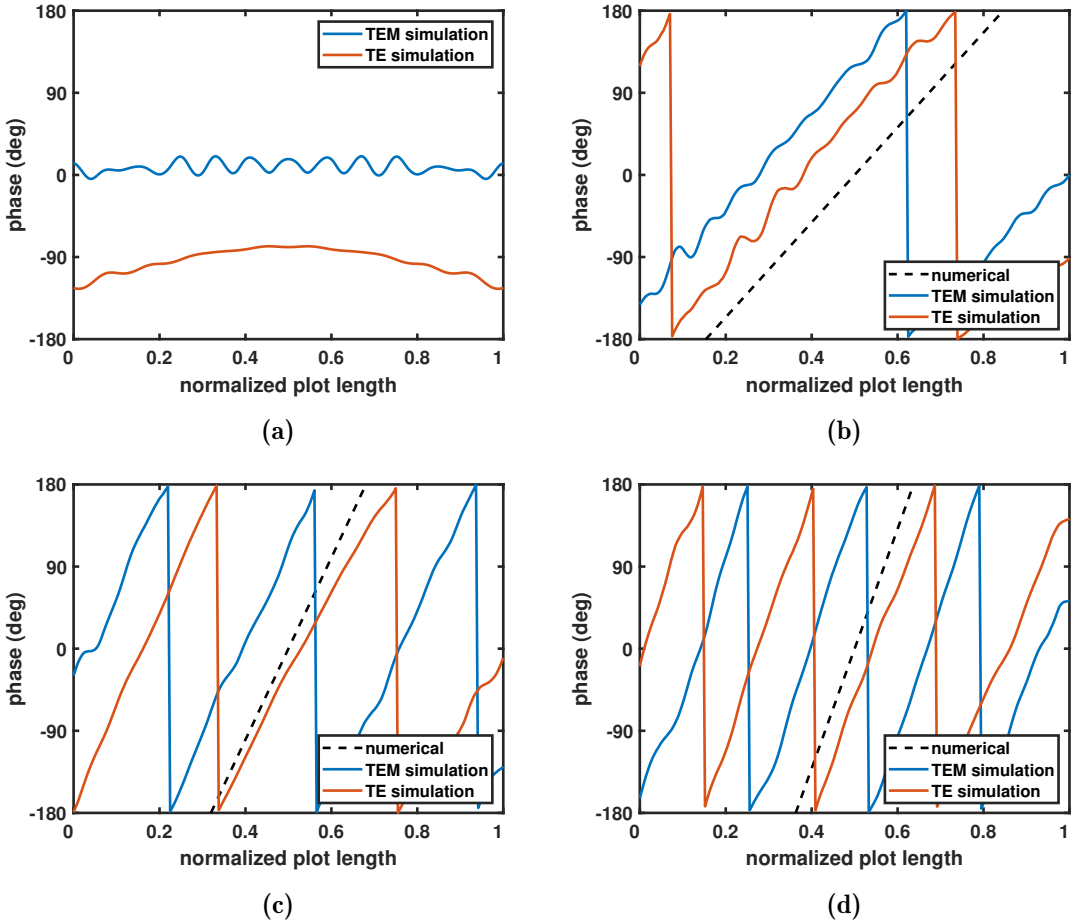

Figure 3.9. Phase profile of the electric field along the plot line (PL) in Fig. 3.1 for TEM and TE_1 modes The black dashed line represents the ideal phase variation for the corresponding pointing direction. The results are derived at the center frequency fc = 29.25 GHz and for a horn displacement (S_h) equal to (a) 0 mm; (b) 30 mm; (c) 60 mm; (d) 80 mm.

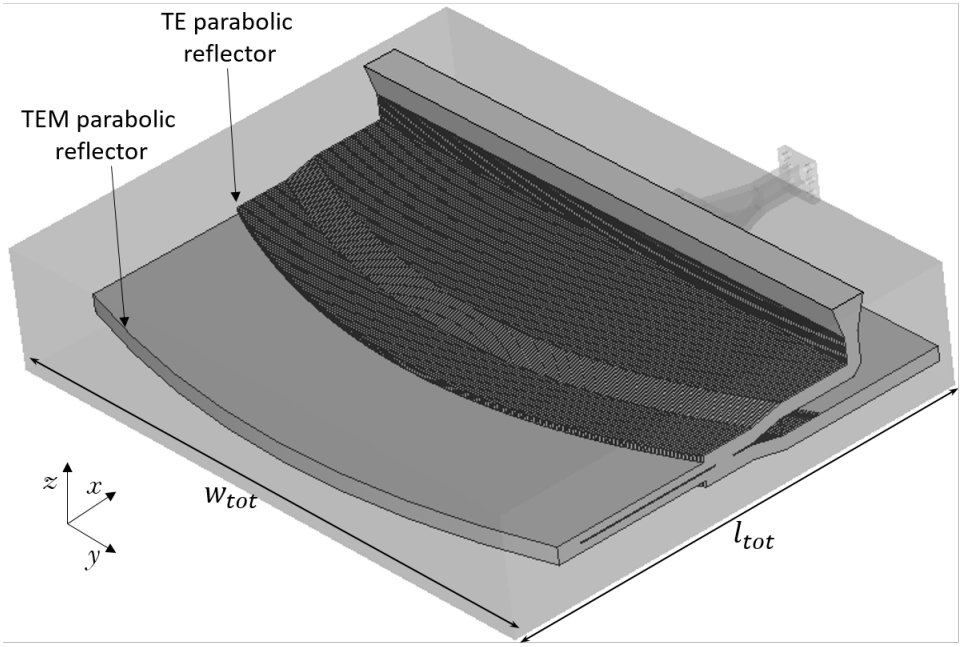

(a)

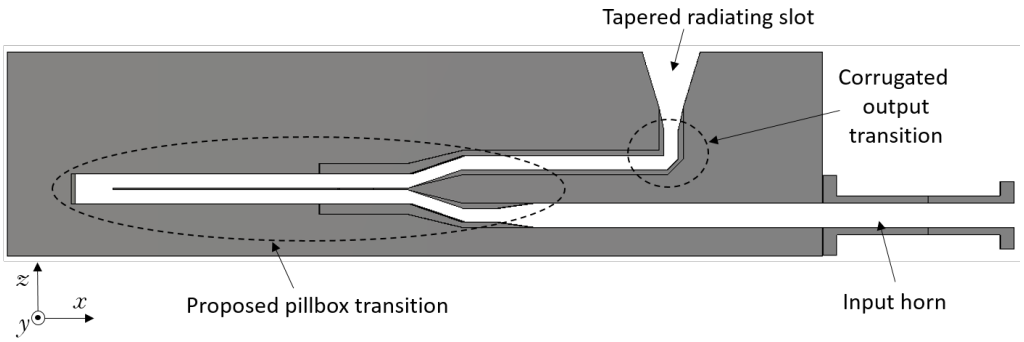

(b)

Figure 3.10. Validation antenna. (a) Prospective view. (b) Sectional view. The full dimensions are $w_{tot} = 300$mm and $l_{tot} = 230$mm.

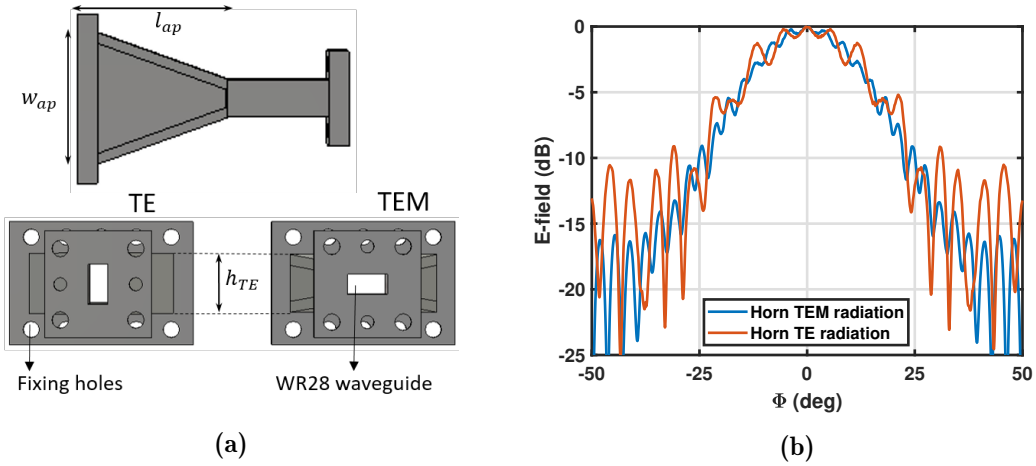

(a) (b)

Figure 3.11. (a) Input horns with dimensions: $l_{ap} = 30$mm, $w_{ap} = 25$mm, $h_{TE} = 7$mm. (b) Electric field radiated by the input horns inside a PPW for the two orthogonal polarizations.

where F is the focal length of the parabolic reflector. $\Delta\Phi_{TEM,TE}$ has been selected to have the best illumination on the parabolas. It is important to notice that the -10dB taperig should be contained always in the parabola profile, even when the input horn is shifted to achieve beamsteering.

3.4.2 Radiating part

The input cylindrical wave is coupled from the pillbox system into a plane wave with a tapered intensity profile. As described before this wave can be used to feed different type of radiating structures. In this antenna, the radiating part is composed by a tapered radiating slot. The transition from the pillbox to the radiating slot has been realized through a 90° bend of the output PPW. Since this PPW can support also TM_1 mode, to avoid its coupling with TEM the two side corrugations are extended from the pillbox output to the radiating aperture. A tapering has been realized on the slot in order to increase the directivity of the antenna. The radiating structure with dimensions is illustrated in Fig. 3.12 (a). Due to the different field distribution of TEM and TE_1 modes the radiation characteristic will be slightly different for the two components. In particular, almost 1dB difference has been computed by simulating the radiating aperture without the full structure. The simulated radiation patterns of the radiating part only are shown in Fig. 3.12(b).

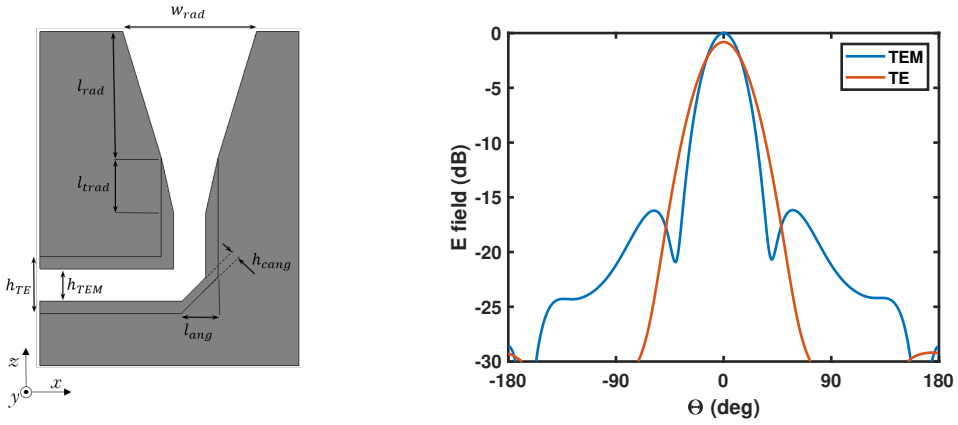

(a) (b)

Figure 3.12. Antenna output part. (a) Section view with dimensions: h_{TE} = 7mm, h_{TEM} = 4mm, l_{ang} = 4.5mm, h_{cang} = 1.05mm, l_{trad} = 6.7mm, l_{rad} = 15.65mm, w_{rad} = 9.55mm. (b) Radiation patterns of the tapered slot for the two modes (xz plane cut).

3.4.3 Full antenna results

The complete antenna illustrated in Fig. 3.10 is analyzed through full wave simulations. The input horns described in section 3.4.1 are exploited to feed the antenna. In particular four different horn shift are considered (S_h): 0mm, 30mm, 60mm and 80mm. Both the excitation modes are considered in this analysis.

In Fig. 3.13 the S11 for the two modes in the different horn positions are reported. It can be observed that the complete antenna achieves a good matching condition (<-11dB) for both the modes in the desired frequency band (27.5GHz - 31GHz). As it is expected, the worst case in terms of reflection coefficient is when the horn is in the focal position (S_h = 0mm). In fact, in this case all the power reflected back from the parabolic transition returns directly inside the feeding horn.

In Fig. 3.14 the resulting radiation pattern are reported. In particular Figures 3.14(a), (b), and (c) illustrates the Φ cut (zy plane) for f_{min} = 27.5GHz, f_{max} = 31GHz and f_c = 29.25GHz respectively. It is possible to observe that in Fig. 3.14(c) the beam direction is the same for both the modes for a certain horn shift. This confirm the analysis of the quasi-optical system described in section 3.3. In fact, the system has been designed to have the same beam shift for the center frequency (f_c = 29.25GHz). Furthermore, also Figures 3.14(a) and (b) respect the beam direction prediction that was previously illustrated in Fig. 3.8. In particular, for lower frequencies (Fig. 3.14(a)) the TE mode radiation has a shift angle lower than the one achieved by the TEM mode. On the other hand, for higher frequencies (Fig. 3.14(b)) the quasi-optical system produces an higher beam shift for the TE

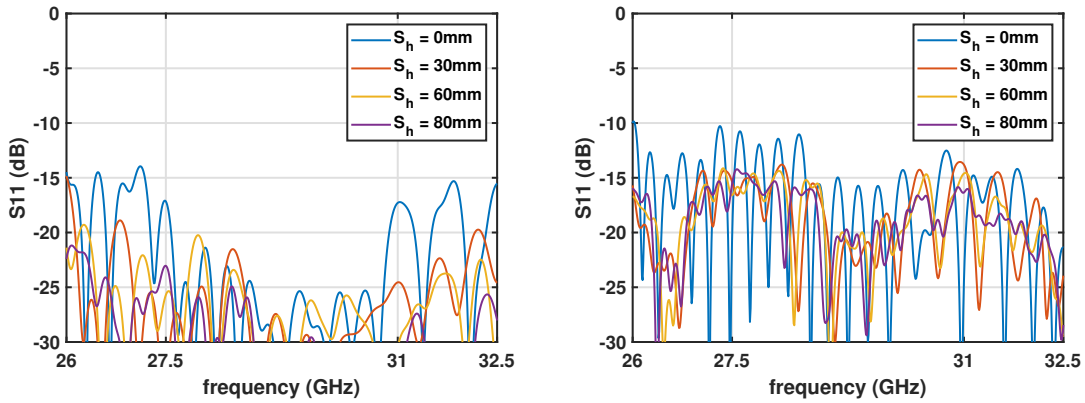

Figure 3.13. S11 simulation results for 4 different input horn positions. (a) TEM results. (b) TE results.

mode.

Fig. 3.14(d) reports the radiation pattern on the Θ cut (zx plane) at the center frequency ($f_c = 29.25$GHz). Here can be noticed the behaviour of the radiating part described in section 3.4.2. In particular, it can be observed that the TE mode achieve a lower gain as previously illustrated in Fig. 3.12(b).

3.5 Conclusions

In this chapter, a novel beamformer is presented. In particular, a pillbox system exploiting multimode transmission is presented. Thanks to that it can be used to feed high gain dual polarized antennas, that are commonly used for space applications. To demonstrate the correct working of the system a dual linearly polarized antenna has been designed and validated through full wave simulations.

In the next chapter an antenna that exploits a pillbox system and is able to radiates in circular polarization is described.

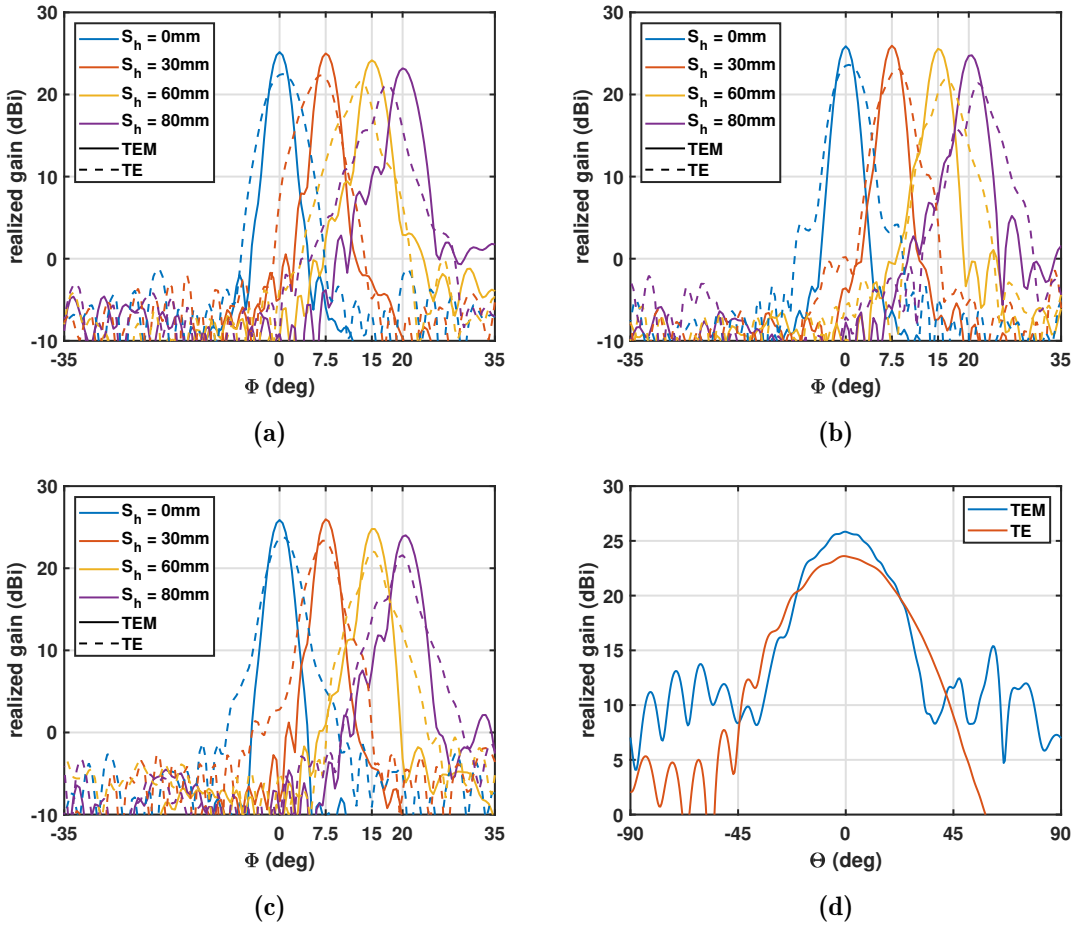

Figure 3.14. Simulated radiation patterns of the complete pillbox antenna for both the mode excitation and different input horn shift. (a) Φ cut (zy plane) at f_{min} (27.5GHz). (b) Φ cut (zy plane) at f_{max} (31GHz). (c) Φ cut (zy plane) at f_c (29.25GHz). (d) Θ cut (zx plane) at f_c for the horn position $S_h = 0$mm.

Chapter 4

Antenna for space applications: Circularly polarized CTS array

As stated in Chapter 3 the growing demand for high-speed satellite communications (SatCom) requires the use of robust and reliable antenna systems. Owing to its capability in mitigating polarization mismatch issues, circular polarization (CP) is a key asset for modern terminal SatCom antennas.

For SatCom communications, the Continuous Transverse Stub (CTS) arrays have gained interest during last decades, due to their broadband, wide-angle scanning and low-profile characteristics [31] [32] [24] [33]. However, their inherent radiation mechanism enables the radiation of linearly-polarized (LP) fields only. To achieve CP radiation, commercial solutions [34] rely on polarizing screens such as the one presented in [35], placed in the proximity of the radiating aperture, thus increasing the complexity, bulkiness and costs of the overall antenna module.

In this Chapter a CTS array, able to radiates in CP, is presented. The radiating structure is composed of dual-mode, open-ended PPWs. In classic CTS arrays [24], these PPWs are designed to work with the dispersionless fundamental mode, i.e., TEM mode. In this work, the radiating PPWs are enlarged to operate in the multi-mode dispersive region, such that the TEM and TE_1 modes can propagate within the radiating structure. As it is shown by the zoomed-in detail in Fig. 4.1, these modes exhibit electric fields orthogonally-polarized with respect to each other [26] and therefore can generate CP radiation [29]. Since the theoretical analysis of the radiation mechanism is fully described in [29], this chapter focuses on the design of an antenna that exploits this principle. The antenna is designed to achieve optimal performances in the SatCom transmission band (Ka-band), i.e., from 27.5 GHz to 31 GHz within a scan range of $\pm 20°$.

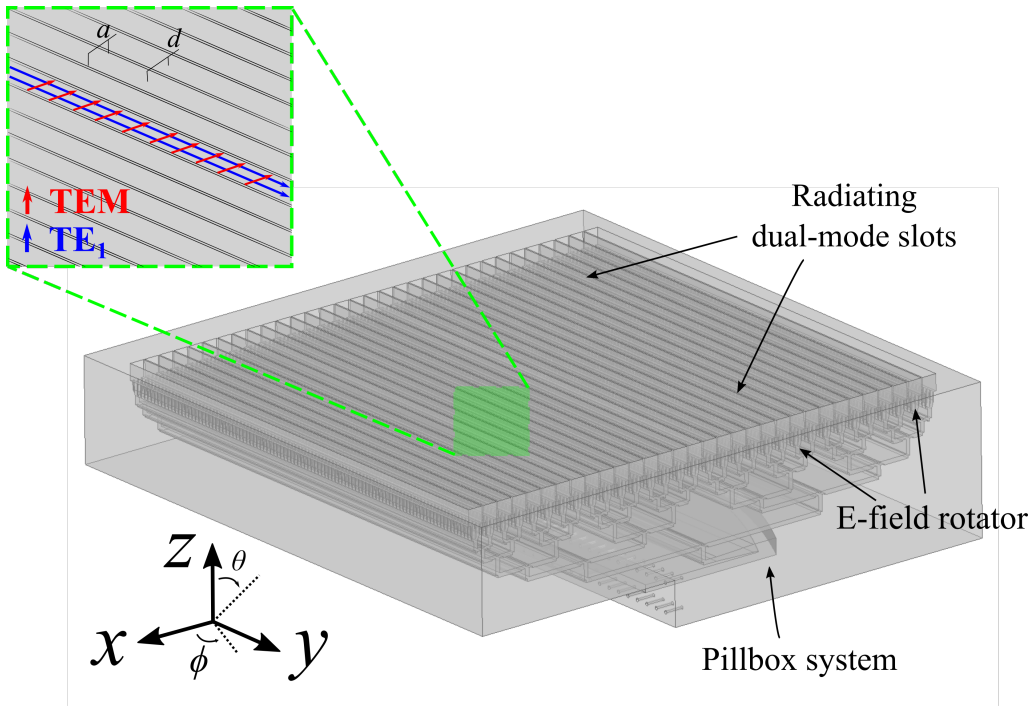

Figure 4.1. Perspective view of the proposed CTS antenna. In the highlighted section the arrows represents the E-field distribution of the TEM and TE_1 modes, a is the height of the radiating PPWs and d is the periodicity of the slots.

4.1 Antenna Architecture

Figure 4.1 shows a perspective view of the proposed antenna. As stated before the radiating PPWs support the propagation of the TEM and TE_1, i.e., $\lambda_{max}/2 < a < \lambda_{max}$ and $\lambda_{max} < 2 \cdot \lambda_{min}$ where λ_{max} and λ_{min} are the maximum and the minimum operating wavelength respectively and a is the height of the PPWs. The multi-modal radiating slots are fed by a pillbox beamformer combined to a PPW based corporate feed and an electric field rotator. To reach an high value of gain, 32 radiating slots have been used.

4.1.1 Pillbox system

The feeding is realized through a pillbox system. This type of quasi-optical structure is fully described in Chapter 3. For this antenna a single-mode pillbox system is used (i.e. $h_{PPW} < \lambda_{min}/2$) . This allows to simplify the feeding mechanism and exploit a previously designed structure. In fact, the Corporate Feed Network (CFN) is designed to be installed on a pillbox system already present in the IETR labs. The structure is described and analyzed in [24]. As a recall from the previous Chap-

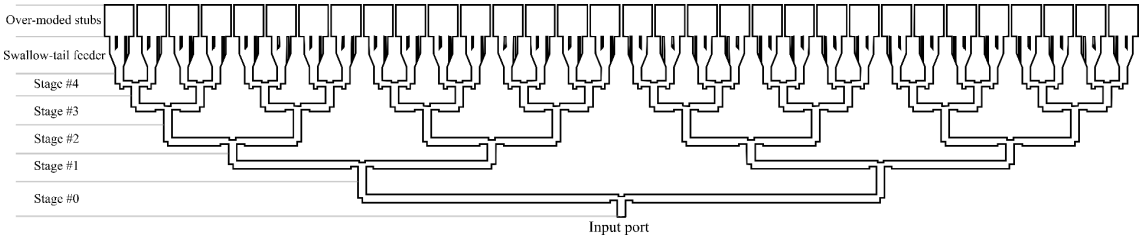

Figure 4.2. Sectional view of the complete corporate feed network. Here the different stages and components are highlighted.

ter, the pillbox beamformer consists of two stacked PPWs, coupled by a parabolic reflector by means of a 180°-bend. A cylindrical wave is launched in the feed layer PPW by the means of a feeding horn placed in the focal position of the parabola. Then, thanks to its quasi-optical behaviour, the pillbox system generates a continuous line source with a tapered E-field amplitude and a progressive phase profile. If the horn is shifted along the focal line of the parabolic reflector, a tilt of the equal phase wavefront can be obtained (see Sec. 3.3). The linear source obtained in the upper layer PPW can be used to feed a CTS antenna array [24]. For this antenna, a parallel fed CTS array is designed. For this reason, the wave generated through the pillbox system is guided inside a 1 to 32 CFN.

4.1.2 Corporate feed network (CFN)

The complete corporate feed network is illustrated in Fig. 4.2. It can be observed that ii is composed by 5 stages of a 1 to 2 way power dividers. This allow to equally splits the power from one input to 32 output slots.

In Figure 4.3(a) the details of the single stage of the CFN is illustrated. In particular, all the CFN is designed with PPWs operating in single mode region, that is $a_{in} < \lambda_{min}/2$). For matching, stepped corners and shrinkage at the input are inserted. In Fig. 4.3(b) the obtained matching of the overall CFN is reported. This results is obtained through full wave simulation. The structure was excited with a Waveguide Port at its input ("Input port" in Fig. 4.2) with a Perfect Match Layer (PML) at the and of the 32 outputs. Despite the complexity of the structure, a good matching condition is obtained in the desired frequency band. The dimensions of the CFN that allowed to achieve this result are listed in Table 4.1 (Dimension labels refer to Fig. 4.3(a)).

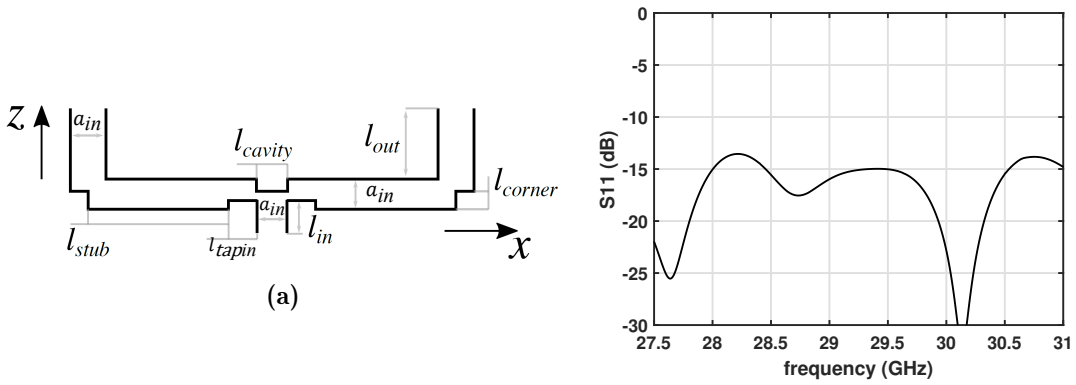

Figure 4.3. (a) Single T-junction sectional view. (b) Input reflection coefficient of the overall corporate feed network.

Stage	l_{stub}	l_{cavity}	l_{in}	l_{out}	l_{corner}	l_{tapin}
#0	60.5	1.39	4.00	3.42	1.17	1.97
#1	28.8	1.39	3.42	2.05	1.17	1.97
#2	12.8	1.59	2.05	3.43	1.07	1.97
#3	4.88	1.59	3.43	2.07	1.14	1.97
#4	0.88	1.59	2.07	n.a.	1.18	1.97

Table 4.1. T-junctions dimensions of the corporate feed. The labels refers to Fig. 4.3 (a). Dimensions are in millimeters.

4.1.3 E-field rotator

The main component of this antenna is the Electric Field Rotator. It is well known from literature [15] that to radiate in CP the E-Fields needs to have two orthogonal components with the same magnitude but with a phase shift of 90° between them (see Sec. 2.3.1 "Feeding ntworks design"). The purpose of this part is to feed the radiating stub with the right E-Fields characteristic in order to achieve a good CP purity.

The designed structure connect the single mode PPW of the CFN with the multimode PPW of the radiating stubs. A perspective view of the component is illustrated in Fig. 4.4. Due to the shape of the middle part of the structure, we decided to name it "Swallow Tail" feeder.

It is possible to divide the feeder in three different sections. The first one, is composed by the single mode PPW of the last step of the CFN. In this part the E-field profile is the one of a TEM mode and it is shown in the cut-plane Σ_3 in Fig. 4.4. As it is stated previously to achieve CP both TEM and TE_1 propagation is needed in the radiating stub. Since this two modes has an orthogonal E-field distribution, the E-field from the CFN needs to be rotated by 45° in order to excite both the modes inside the radiating stub with the same amplitude. This effect is obtained by exploiting the central portion of the structure. This part, with the Swallow Tail shape, combines an increment of the PPW height with a gradual formation of a 45° inclined grid. The E-field distribution in this section can be observed in the cutting plane Σ_2. Finally, the E-Field profile plotted on the cutting-plane Σ_1 shows that the designed feeder achieves the desired E-Field distribution at the start of the last part, the radiating stub.

In Figure 4.5(a) the simulation setup of the Swallow Tail feeder is illustrated. It has been analyzed with an infinite structure obtained through periodic boundaries conditions. A waveguide port exciting the TEM mode was placed ad the end of the CFN network (input of the E-Field rotator). If the radiation characteristics needs to be verified, a Floquet port can be placed on a open boundaries condition, as it is shown in Fig. 4.5(a). On the other hand, in order to analyze the correct power splitting between the two modes in the radiating stub, a second waveguide port has been placed at its open end. The results of this set-up, in terms of S-parameters are reported in Fig. 4.5(b). The plot shows that the Swallow Tail feeder is perfectly matched (S11<-15dB) in the whole Ka-band. Furthermore, the power between the modes is equally split as it can be stated by the S21 values of -3dB.

As it is stated before, to radiate in circular polarization, a phase difference be-

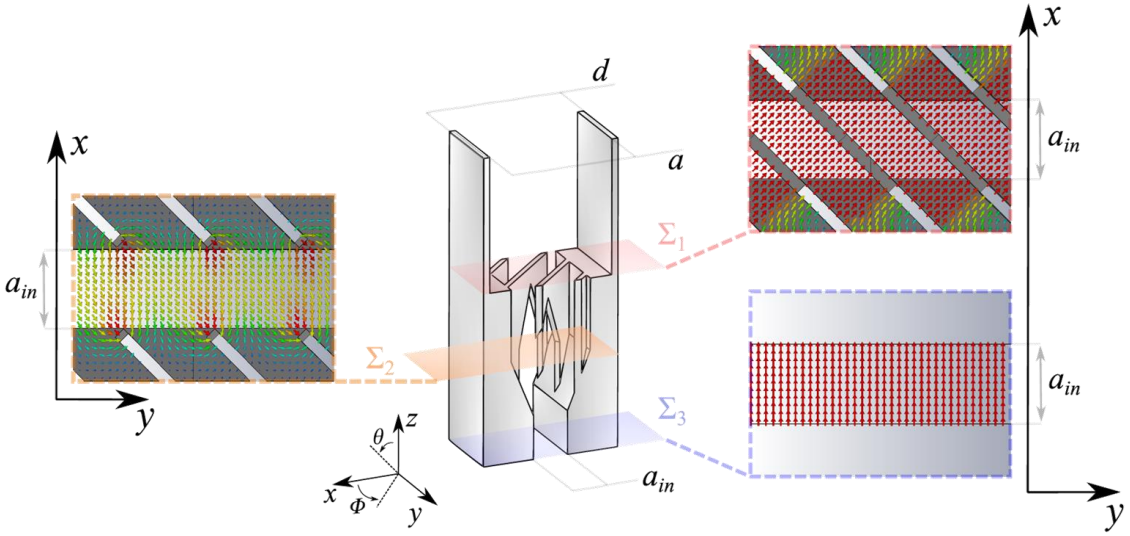

Figure 4.4. Perspective view of the "Swallow Tail" E-field rotator. The E-filed vector plots on three different cut planes are shown.

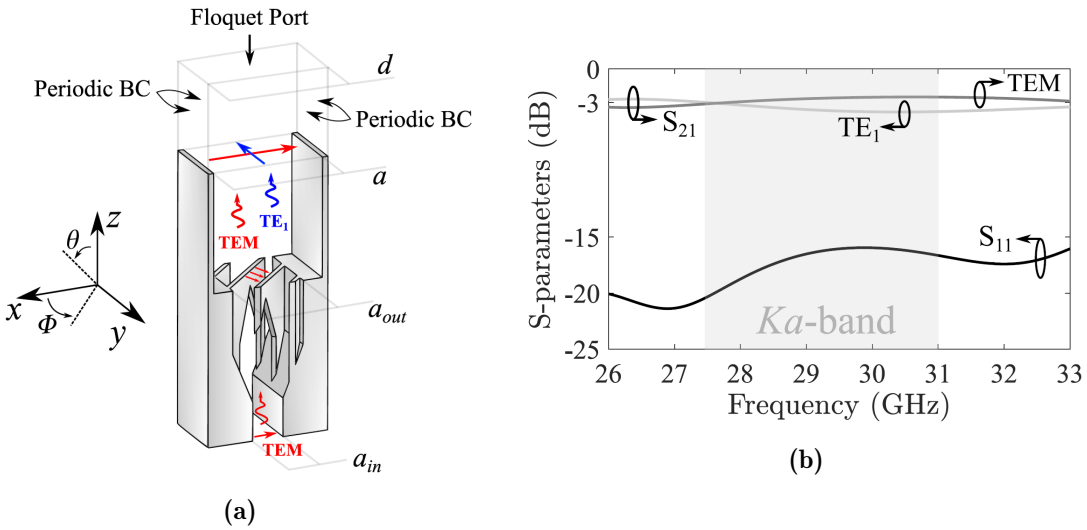

Figure 4.5. (a) Unit cell simulation setup of the E-field rotator. (b) S-Parameter simulation results of the E-field rotator unit cell.

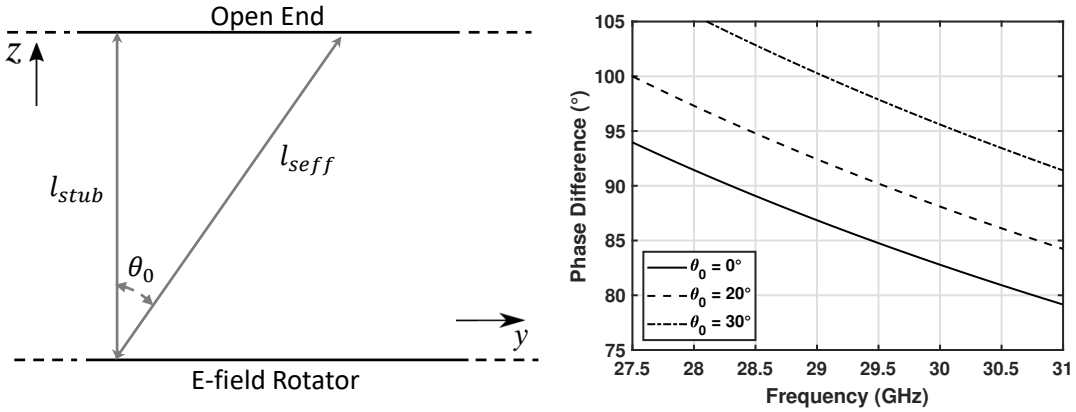

(a) **(b)**

Figure 4.6. (a) Schematic representation of the geometrical path of the wave inside the open-ended stub. (b) Phase difference between the TEM and TE_1 modes at the open end of the stub for three different angle of steering.

tween the TEM and the TE_1 modes is needed. Since the two modes propagates with a different phase velocity inside the radiating stub, it is possible to engineer the length of the stub to have the desired phase difference at the aperture. In particular β_{TEM} and β_{TE_1} inside a PPW can be computed with equations (3.2) and (3.4) respectively. The total phase shift of the modes can be calculated as

$$\Delta\varphi_{TEM,TE} = l_{stub} \cdot \beta_{TEM,TE} \tag{4.1}$$

thus, the Phase Difference (PD) is

$$PD = \Delta\varphi_{TEM} - \Delta\varphi_{TE}. \tag{4.2}$$

The PD computed with equations (4.1) and (4.2) is true if we consider the direct path from the 45° grid to the open end of the stub. When a tilt of the wave occurs (θ_0) the effective length (l_{seff}) of the path inside the stub is different. This concept is illustrated in Fig. 4.6(a). The value of l_{stub} in equation (4.1) should be replaced with

$$l_{seff} = \frac{l_{stub}}{cos(\theta_0)}. \tag{4.3}$$

The PDs obtained with a PPW height of 7.2mm and a l_{stub} of 8.2mm for three different tilt angles in the desired band are illustrated in Fig. 4.6(a). A trade off between a good CP purity at broadside direction and the maximum scanning angle needs to be made. Mainly for this reason this antenna will keep a good CP purity for a scanning angle up to $\theta_0 = 20°$ but it will degrade for a higher angles.

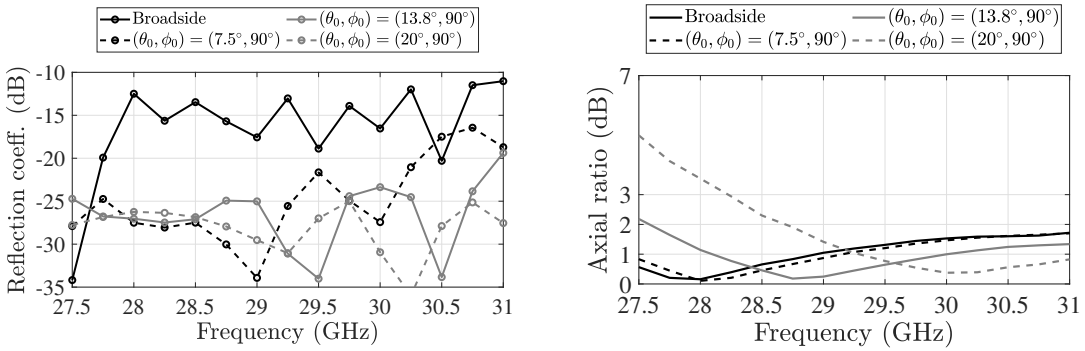

Figure 4.7. (a) Simulated reflection coefficient of the proposed CTS antenna for 4 different scanning angles in elevation along the yz-plane in Fig. 4.1. (b) Simulated axial ratio of the proposed CTS antenna for 4 different scanning angles in elevation along the yz-plane in Fig. 4.1.

4.2 Complete Antenna Performances

All the component previously described are combined together and the complete antenna has been analyzed through full wave simulations [36]. The performances are analyzed for four different scanning angles θ (that correspond of four different feed horn position see Sec. 3.3) along with the azimuthal yz-plane: broadside, 7.5°, 13.8° and 20°. Due to the symmetry of the structure on the xz-plane the obtained results can be extended to specular direction (-7.5°, -13.8°, -20°). In Fig. 4.7(a), the reflection coefficient versus the frequency is reported. The antenna achieve a good matching condition (i.e. $<$ -10 dB) over the entire band. Furthermore, thanks to the high number of radiating slots, a gain higher of 32 dBi is achieved. It can be noticed that, since a pillbox beamformer is used for the feeding system, the worst matching condition occurs when the feeding horn is in the parabola focus position, i.e. for broadside radiation.

To verify the CP purity the AR is plotted in Fig. 4.7(b). In particular the CP is here considered acceptable for AR smaller then 3 dB. The AR remains below the 3 dB threshold over the whole frequency band for scanning angles up to $\theta = 14°$. When $\theta = 20°$, the AR is above 3 dB in a small portion of the band. For higher angle of scanning the AR will increase its value due to the geometrical path in the stub as it is explained in Sec. 4.1.3.

Finally, in Fig. 4.8 the simulated radiation patterns for two different scanning angle are illustrated. The reported results are obtained considering the Right Hand Circular Polarization (RHCP). In both cases the anenna demonstrates a very good

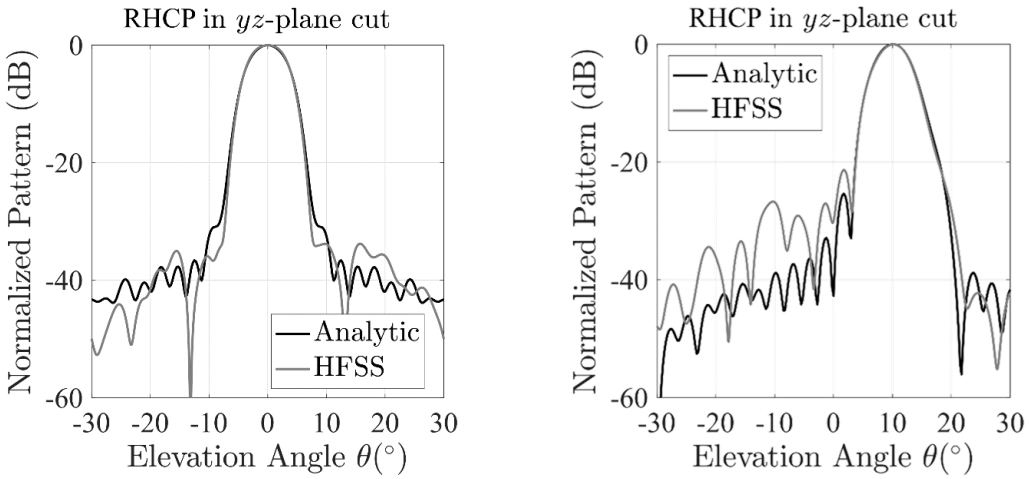

Figure 4.8. (a) Simulated radiation pattern in RHCP for the broadside direction. (b) Simulated radiation pattern in RHCP for $\theta = 10°$.

performance with a Side Lobe Level less than -20dB.

4.3 Conclusions

In this chapter a novel antenna for SatCom applications is presented. The proposed antenna is based on the parallel-fed CTS architecture and it is able to radiate CP fields without using any external devices. High-gain, optimal matching, and a large 3-dB-AR bandwidth are achieved in the Ka-band for angles of scanning up to $\pm 20°$. The presented solution allows to save costs and space and offers valid alternative respect to commercial SatCom terminal antennas.

This chapter concludes the study performed on SatCom systems. In the next chapter a mmW antenna module suitable for the automotive market will be presented.

Chapter 5

Automotive 5G mmW antenna Module

In this chapter, an automotive antenna module suitable for the 5G communications in the mmW frequency band is presented. Since this type of communication is new for the market, there aren't available benchmarks or examples. Furthermore, the car manufacturers don't have a clear idea on the requirements and specification needed. For this reason an analysis of the standards is necessary to understand the key parameters of the mmW 5G communications and relate them to the car industries. After this first study on requirements a possible radiating element solution is designed and prototyped. Finally, a complete module comprising the electronic is presented.

5.1 Requirements and constrains

The main regulatory institution about the cellular communication is the Third Generation Partnership Project (3GPP). From release 15 the 3GPP starts to standardize the 5G communications. From the released files is possible to extracts the desired informations. Two main topics are of interest for the design of an antenna: its working frequency and its output power.

The standard divides the 5G frequencies in two ranges the Frequency Range 1 (FR1) and the FR2. The FR2 is the one containing the mmW frequency range. Figure 5.1 [37] reports the allocated frequencies for the FR2 around the world. This Range is itself divided in 3 bands: the n257 from 27.5GHz to 29.5GHz, the n258 from 24.25GHz to 27.5GHz and the n261 from 27.5GHz to 28.35GHz. This definition allows a first estimation of the necessary antenna bandwidth (BW). If the whole FR2 is covered a 19.5% BW is required.

It is well known that the attenuation at high frequency is higher, for both what

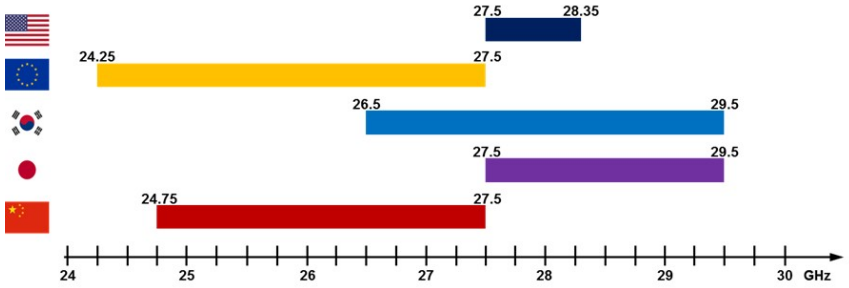

Figure 5.1. Allocated frequency in the FR2 frequency band around the world.

concerns the free space attenuation and the obstacle attenuation. For this reason, in order to cover an acceptable distance, the total gain of the antenna needs to be increased. This can be done by enhancing the antenna directivity and by increasing the output power. The standard sets the maximum powers for the antenna. In particular in Tab. 5.1 are listed the maximum power values for a "Power Class 2" equipment (i.e. everything that is not a base station) [38]. The power levels are expressed in terms of Total Radiated Power (TRP) and Equivalent Isotropic Radiated Power (EIRP). If we consider an antenna array of n elements in which each element is connected to a Power Amplifier of gain PA_{pout} the TRP is defined as

$$TRP(dBm) = PA_{pout} + 10log_{10}(n). \tag{5.1}$$

On the other hand, the EIRP takes into account also the antenna directivity. If the single antenna element has a realized gain of Ga, the EIRP can be computed as

$$EIRP(dBm) = PA_{pout} + 10log_{10}(n) + Ga_n + 10log_{10}(n). \tag{5.2}$$

An analysis of commercial available MMICs (Monolitic Microwave Integrated Circuits) (e.g. Anokiwave, Analog Devices, Integrated Device Technology, Qorvo) has been conducted. Among them PA_{pout} value is 19dBm maximum. It is then possible to compute the number of antenna elements necessary to reach the maximum EIRP. If a 8 element antenna array is considered with a single element gain of Ga = 6dBi (reasonable for example in the case of a patch antenna) from eq. 5.2 we have EIRP = 43dBm.

We stated that in order to transmit enough power we need an antenna array of at least 8 element. When the antenna directivity increase, as a consequence, its main lobe aperture will reduce. For this reason the main beam needs to change its direction real time, with the car movement. This behaviour can be obtained exploiting the phased array theory [15]. For our application we decided to use an electronically scanning array. In this type of antennas the phase of each element

Operating Band	Max TRP (dBm)	Max EIRP (dBm)
n257	23	43
n258	23	43
n261	23	43

Table 5.1. Maximum powers allowed by the standard at mmW frequencies (FR2).

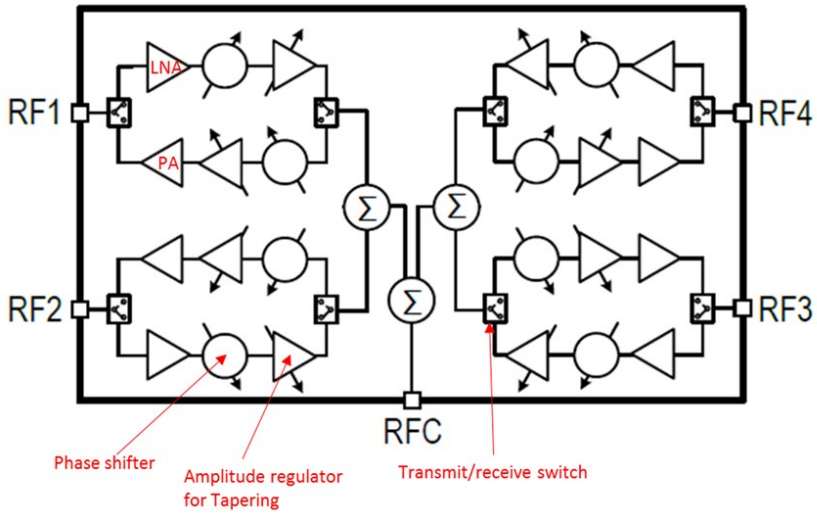

Figure 5.2. Block diagram of the internal components of modern MMIC.

is controlled by an electronic phase shifter causing constructive interference in the desired direction. Modern MMIC integrates on the same chip all the necessary components for the management of an antenna array (e.g. Power Amplifiers, LNA, Phase Shifters ecc). In Fig. 5.2 a generic block diagram of a modern MMIC is illustrated.

For what is concerning the installation on the vehicle we have to consider that the main requirements is to cover all the direction around the car. For the purpose, four modules can be installed on all the sides of the vehicle. Each module needs to cover at least $\phi = \pm 45°$ on the azimuthal plane. On the other hand, to counteract the uphill/downhill condition, at least $\theta = \pm 25°$ is needed on the elevation plane. This concept is illustrated in the schematic representation of Fig. 5.3. It is important to highlight that, to respect aesthetic requirements, the antenna module should be low profile as possible.

Finally, consideration about the antenna radiation polarization can be made. For this work we decided to design radiating elements able to radiates in double linear polarization. This feature can be useful to create a more robust system against the multipath scattering. Moreover, in case of good signal strength for both the

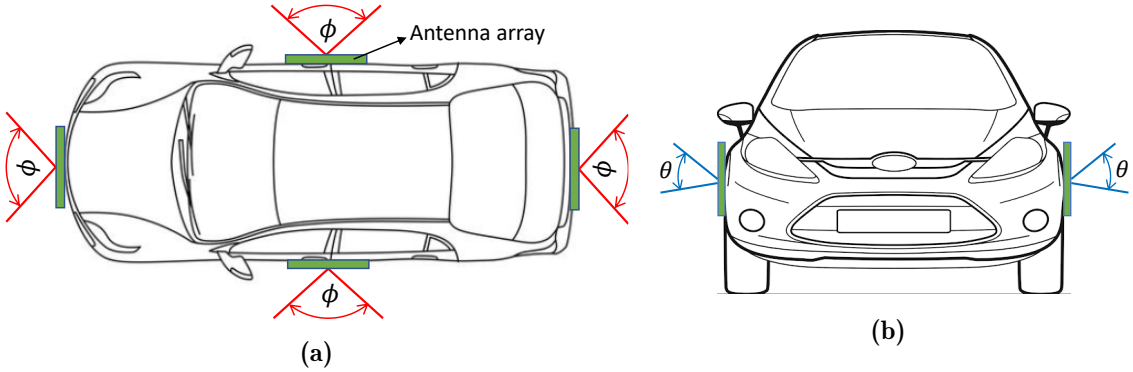

(a) (b)

Figure 5.3. Schematic representation of the mmW antenna modules installation on the car. (a) Top view. (b) Front view.

polarization it can be used as a diversity characteristic for a MIMO system.

To resume, to cover all the described requirements an antenna array is necessary. This array needs to match a relatively high BW and radiates in double linear polarization. Since the commercial electronics are made to cover only a small portion of the FR2, we decided to design the array in the n258 band (i.e. the EU band). Furthermore, once it is installed on the car an azimuthal coverage of $\phi = 90°$ and an elevation radiation of $\theta = 50°$ is required. In order to accomplish these features, we decided to design a PCB antenna array able to scan on the azimuthal direction and with a fixed beamwidth on the elevation cut. The array will be composed by a row configuration with 8 radiating elements, that is enough to reach the desired radiated power. Furthermore, the PCB technology allows to realize a low profile radiating element and to combine it easily with the feeding electronics (e.g. MMIC).

5.2 Radiating element design

In this section we focus our attention on the design of the radiating elements and the array configuration. The focus is to reach the previously described requirements in terms of frequency range and radiation characteristics. The interaction with the electronics will be taken into account in the next one.

5.2.1 Design and simulations

The array is composed by 8 patch antennas placed in a 1x8 configuration. Patches antenna, since they are a resonant structure, typically doesn't reach a wide BW behaviour. Common techniques for increasing the BW are the increment of the substrate thickness [39] or imposing the formation of a second resonance with a

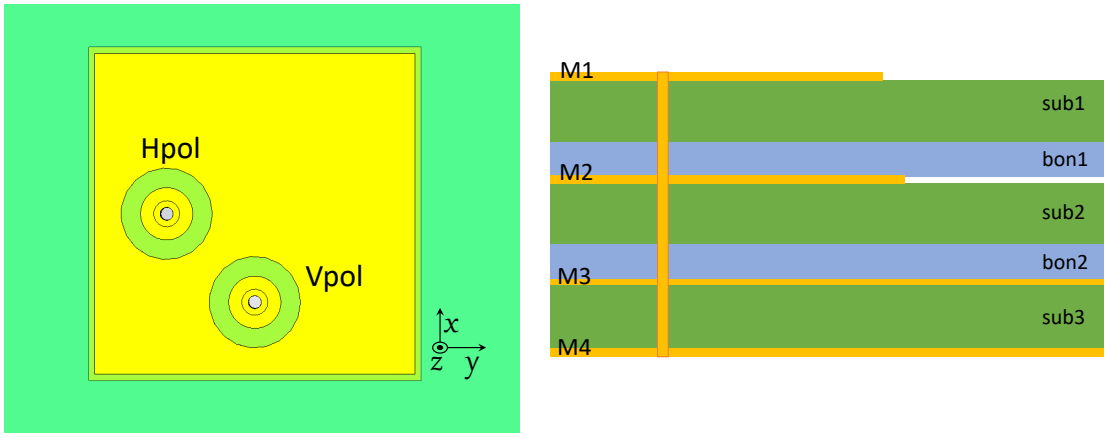

(a) **(b)**

Figure 5.4. (a) Single radiating element. (b) PCB stackup, M_n indicates the metal layers, sub_n are the substrate layers while bon_n are the prepreg layers. Layers are described in Tab. 5.2.

parasitic element [40] [41]. In our case, to reach the desired bandwidth a stacked patch parasitic element is added above the radiating patch [42]. To increase the BW the stacked patch needs to have a different resonant frequency respect to the main one. For this reason they have slightly different dimension. Main patch resonant length (L_{main}) = 2.6mm, Stacked patch resonant length ($L_{stacked}$) = 2.45mm. Furthermore, since a double linear polarization is required, the patch is designed with a square dimension. This solution allows to achieve a symmetric radiation for both the polarizations. The structure of the single element is illustrated in Fig. 5.4(a). The PCB stackup is illustrated in Fig. 5.4(b).

The feeding line, realized with microstrips is on metal layer M4, the patch is on M2 and the stacked parasitic element lies on M1. The metal layer M3 act as a ground plane. The feed is realized through a vias connecting the microstrips on M4 to the main patches on M2. In order to keep the production costs as low as possible only through vias are exploited. For this reason, the feeding vias need to be isolated on the stacked element on layer M1. The isolation can be clearly observed in the single element detail in Fig. 5.4(a). The figure highlights also the two feeds for the horizontal polarization (H pol, y oriented) and the vertical polarization (V pol, x oriented). A synthetic description of the layers is provided in Tab. 5.2. The PCB is designed using low loss high frequency materials [43]. In particular, the RO4350BLoPro (Dk = 3.56 and tand = 0.0037 @ 10GHz) has been used as a substrate dielectric laminate. The selected prepreg material is the RO4450F (Dk = 3.52 and tand = 0.004 @ 10GHz) that shows similar dielectrics characteristics to the

Layer	Name	Material	Thickness (mm)	Description
1 (TOP)	M1	Copper	0.017	Stacked patch
2	sub1	RO4350BLoPro	0.271	Stacked patch substrate
3	bon1	RO4450F	0.102 x 2	Stacked patch substrate
4	M2	Copper	0.017	Main patch
5	sub2	RO4350BLoPro	0.271	Main patch substrate
6	bon2	RO4450F	0.102	Main patch substrate
7	M3	Copper	0.017	Ground Plane
8	sub3	RO4350BLoPro	0.271	Microstrip substrate
9 (BOT)	M4	Copper	0.017	Microstrip feed line
1-9	vias	Copper	0.2 (diameter)	Feed connection

Table 5.2. Layers description of the PCB stackup illustrated in Fig.5.4(b).

main substrate material.

The single element correct working has been verified with numerical simulation. In particular, since the interaction with the other element needs to be considered, the structure illustrated in Fig. 5.4(a) has been studied with periodic boundaries condition. The spacing between the elements is designed such as no grating lobes occurs at the maximum scanning angle $\phi = 45°$. The Active Reflection Coefficient (ARC) [44] results for three different scanning angle are reported in Fig. 5.5(a). The matching is below -10 dB for both the polarizations over the whole n258 band. In the limit case of a scan angle of $\phi = 45°$ the ARC is slightly higher than the -10dB threshold for a small portion of the band but is still acceptable. In Fig. 5.5(b) the radiation pattern simulation results on the azimuthal cut at 26GHz are reported. The results shows an acceptable behaviour in terms of sidelobe level (i.e. $<$ -12 dB) also in the case of $\phi = 45°$ beam shift.

After the simulation under the unit cell condition, the real configuration of the 1x8 array has been considered. The simulation setup is illustrated in 5.6(a). For what is concerning the ARC and the radiation pattern on the azimuthal plane, not strong differences has been noticed respect to the results presentend in Fig. 5.5. On the contrary, the elevation plane radiation patterns shows a strong deformations. The results are displayed in Fig. 5.6(b). In the plot is possible to notice how a strong ripple appears on the radiation characteristic of the vertical polarization. This affect can be ascribed to a surface wave propagation on a finite ground plane [45]. In fact, since we need a relatively high BW, the dielectric slab composed by the substrate is designed thick respect to the wavelength. This causes a propagation of

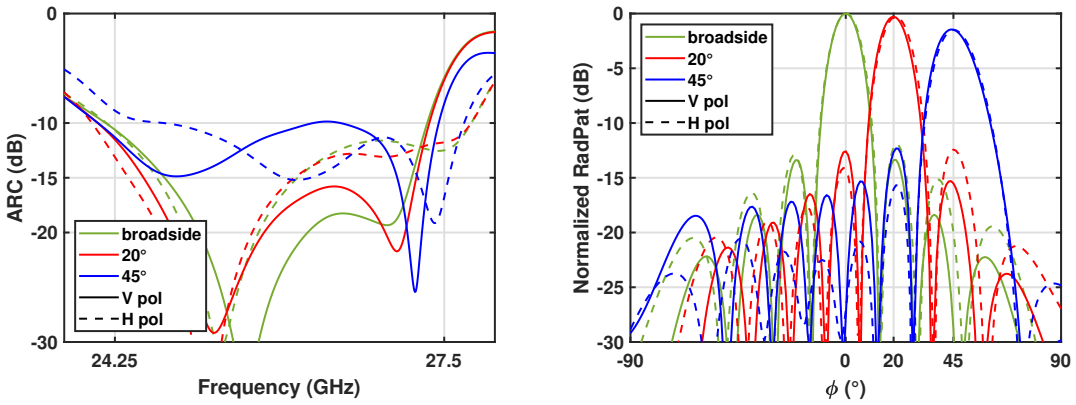

(a) (b)

Figure 5.5. (a) ARC simulation results at three different scan angles, broadside, $\phi = 20°$, $\phi = 45°$ for both the polarizations. (b) Simulation results of the radiation pattern on the azimuthal plane ϕ at 26GHz.

waves inside the substrate, travelling between the patches ground plane and the air. Since it is an evanescent wave, it will radiates causing a radiation pattern distortion proportional to its space of propagation. In Fig. 5.6(a) it is possible to observe that the ground plane relative to the V pol (GND_x) is bigger than the one relative to the H pol (GND_y). This dimensional difference makes the surface waves causing a distortion only in the V pol radiation. It can be observed a ripple oscillation of 5dB that it is not acceptable for our application.

A possible solution for the radiation pattern distortion can be the reduction of the ground plane dimension. Unfortunately a physical size reduction is not possible because of the space needed for the electronic installation. For this reason an "electromagnetic" size reduction is implemented.

5.2.2 Electromagnetic Band Gap (EBG) structure

The "electromagnetic" size reduction previously illustrated is obtained through an Electronic Band Gap (EBG) structure. EBGs are periodic structures that behaves as a high impedance surface for electromagnetic waves. If correctly designed, it is possible to change the dielectric-air interference conditions creating a forbidden, or Band Gap (BG), frequency region in which the undesired surface waves cannot propagate. In this first part of the work we decided to exploit a mushroom like structure [46]. This structure is composed by a square patch (laying on M1) connected to the ground plane (M3) by a shorting via. Also in this case only through vias are exploited. The unit cell is illustrated in Fig. 5.7(a). The frequency behaviour of

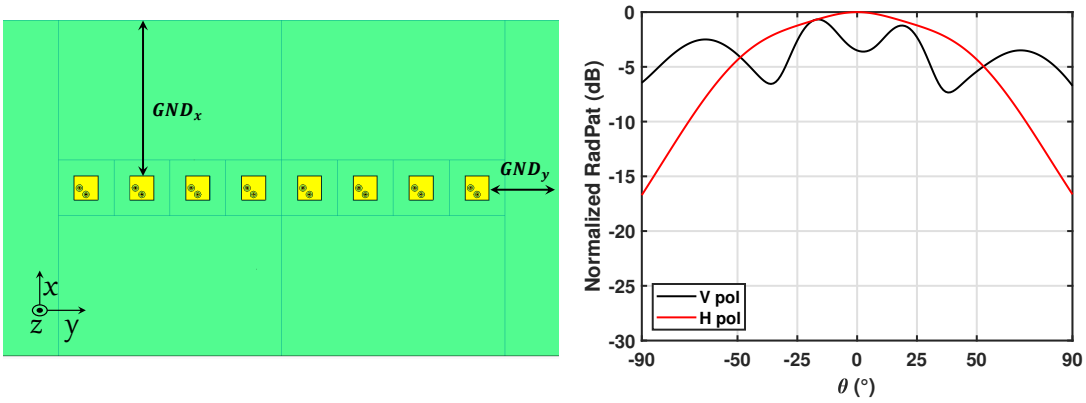

(a) (b)

Figure 5.6. (a) Simulated 1x8 array configuration. (b) Simulation results of the radiation pattern on the elevation plane θ at 26GHz.

the structure is studied exploiting the eigenmode solver. The resulting dispersion diagram is illustrated in Fig. 5.7(b). Black dashed lines highlight the band gap achieved, that is from 22 to 32 GHz. The BG lower bound is is set by the maximum propagation frequency of the first mode. On the other hand, the upper bound is limited by the crossing of the "ligthline" by an higher order mode.

Through simulations we observed that 6 repetitions of the unit cell along the propagation direction are enough to suppress the surface wave propagation. The array 1x8 array module including the EBG structure is simulated. The model can be observed in Fig,5.8(a). The simulation results of the radiation patterns on the elevation cut are reported in Fig.5.8. Here, from black solid line can be observed how the undesired ripple is mitigated thanks to the EBGs. It can be also observed that the achieved gain from the V pol is now higher than the H pol. This effect occurs because the two regions with the EBG structure act as a wall for the vertical fed patches. Thus, the V pol radiating elements can be considered operating in structure similar to a cavity backed patch antenna [47]. This type of structure is known to increase the gain of the radiating element [48]. However, for both the polarizations the requirement of an elevation aperture grater of $\theta = \pm 25°$ is accomplished.

5.2.3 Prototype and experimental results

To verify the correct working of the designed array a prototype has been fabricated. In order to measure the realized gain broadside, the antenna is fed through a Corporate Feeding Network (CFN) that equally splits the power between the elements. The CFN connects the 8 elements to a single input through 3 cascaded T-junctions.

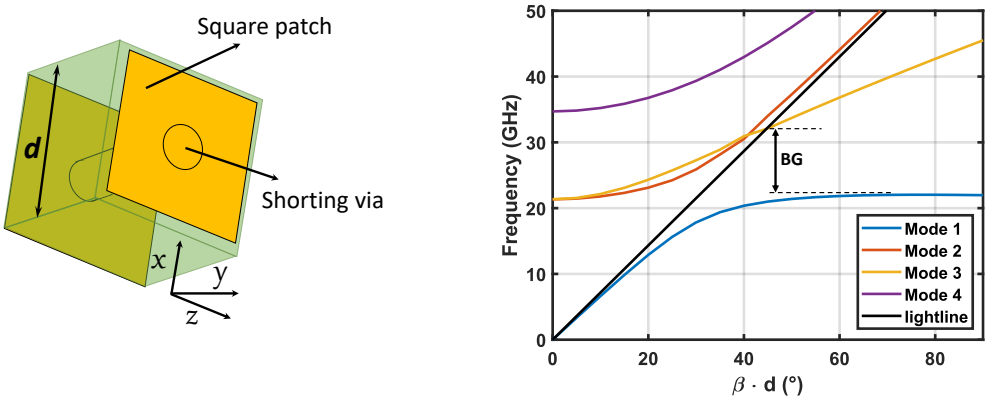

(a) (b)

Figure 5.7. (a) Simulated unit cell of the EBG mushroom structure. (b) Dispersion diagram of the designed EBG structure, the obtained Band Gap from 22GHz to 32GHz is highlighted.

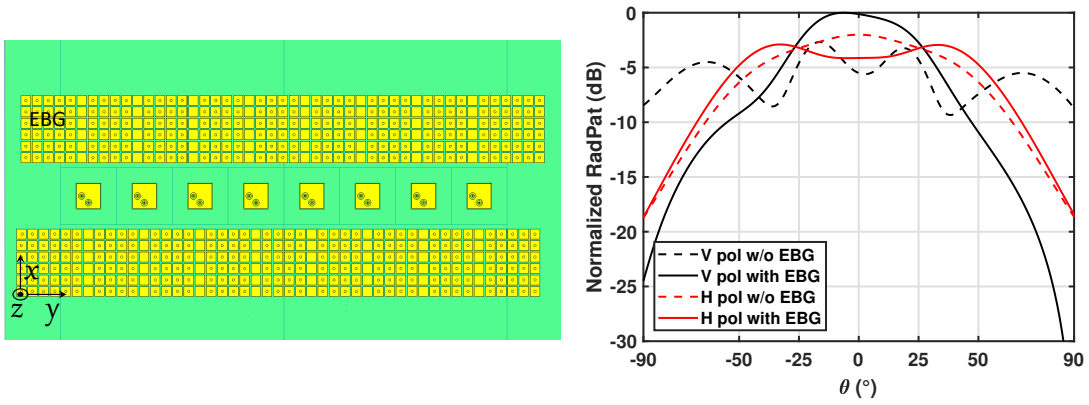

(a) (b)

Figure 5.8. (a) Simulated array structure with EBG. (b) Comparison between the simulation results of the radiation pattern on the elevation plane θ at 26GHz of the array with and without EBG.

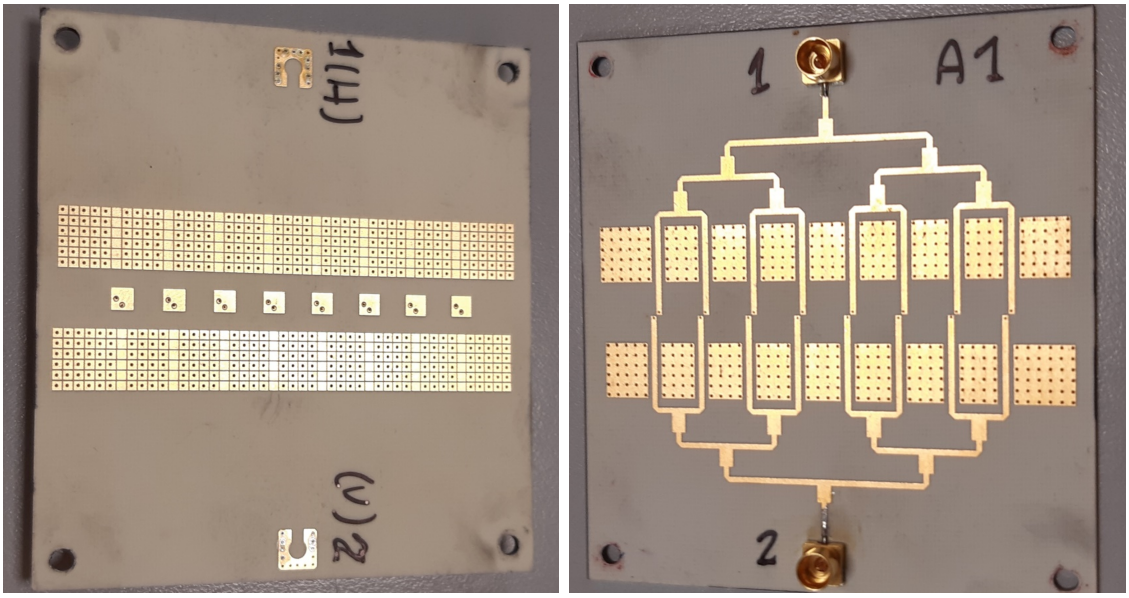

(a) **(b)**

Figure 5.9. Picture of the fabricated prototype. (a) Antenna side. (b) Feeding network side.

The lines have the same length so the elements achieves broadside radiation. The antenna is fed exploiting a SMP connector. In Fig. 5.9 the pictures of the fabricated prototype are shown. In particular, the picture in Fig. 5.9(a) shows the antenna side of the PCB where the patches and the EBG are visible. On the other hand Fig. 5.9(b) shows the feeding network layer.

The prototype has been tested and measured in an mmW anechoic chamber. Results in terms on S-paramaters for both the polarizations are reported in Fig. 5.10(a). Here is possible to observe that the array achieves a good matching condition (<-12dB) for both the V pol and the H pol in the derided frequency band. Also, the coupling between the two remains low (<-20dB) ensuring a good cross polarization (X pol) isolation. In Fig. 5.10(b) the realized gain of the array is reported. The illustrated gain measurement results refers to broadside radiation (i.e. $\phi = 0°; \theta = 0°$). The graph shows that the antenna achieves a gain near to 12.5dBi for both the polarizations until the 25GHz. After this frequency the H pol gain starts to decrease (reaching 10dBi at 27.5GHz) and the V pol gain starts to increase (reaching 14dBi at 27.5GHz). This behaviour is due to the cavity-backed patch antenna effect described in the previous section.

The effect produced in the radiation characteristics by the EBG structure is highlighted also in Fig. 5.11(a). Here, the measured elevation cut of the radiation pattern is reported. It is possible to notice that the measurement results are in good

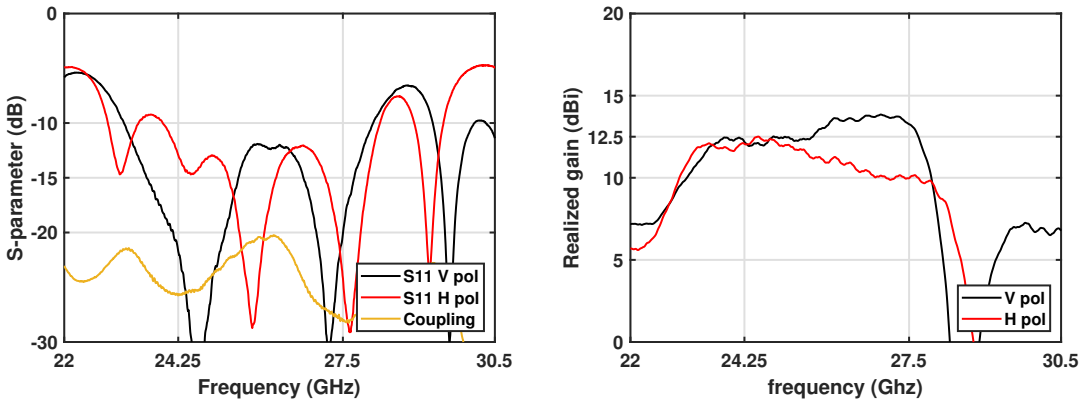

(a) **(b)**

Figure 5.10. (a) Measured Sparameters on the realized prototype. (b) Measured realized gain broadside on the fabricated prototype.

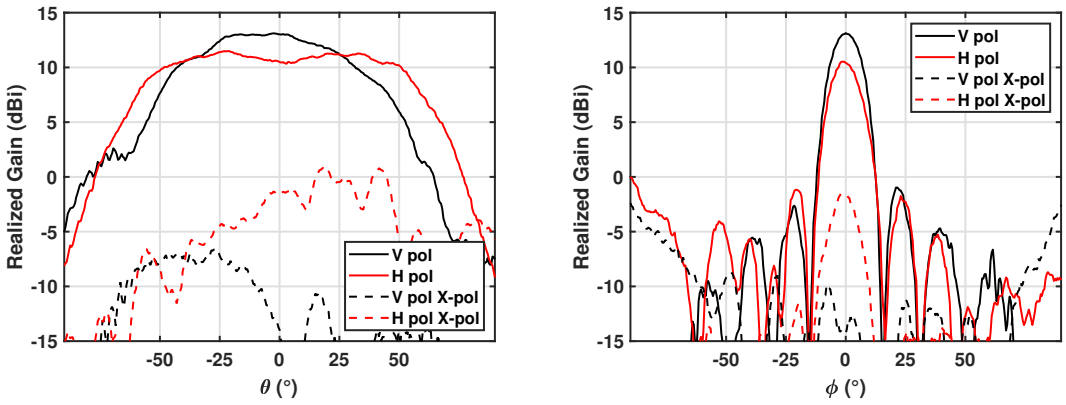

(a) **(b)**

Figure 5.11. (a) Measured radiation pattern on the elevation plane θ at 26GHz. (b) Measured radiation pattern on the azimuthal plane ϕ at 26GHz.

agreements with the simulation results showed with solid lines in Fig. 5.8(b). In fact, at 26GHz, the radiation pattern presents a increment of gain for the V pol and a slight deformation for the H pol. In Fig. 5.11(b) the azimuthal cut of the measured radiation pattern at 26GHz is reported. The observed sidelobe level is <-12dB. The figures show also the X pol radiation patterns (dashed lines. The X pol levels measured remains below 10dB in the worst case.

5.3 Complete 5G antenna module

In this section the PCB that includes the radiating elements previously described is integrated together with the electronic. The MMIC selected for our application is the Anokiwave AWMF-0165. It can control up to 4 radiating elements in double polarization. Furthermore, its frequency range covers all the n258 band from 24.25GHz to 27.5GHz. The description of all the connection (e.g. supply, digital) of the complete module is out of the scope of this thesis.In particular, this section will go through the description of the RF solution implemented in the complete PCB.

5.3.1 MMIC integration

A PCB board has been designed to manage the supply voltage and the digital connection for the MMIC programming. The complete PCB can be described as the superposition of the "Antenna board" and the "MMIC board". This concept is highlighted in Fig. 5.12(a) where the sectional view of the complete PCB is shown. The "Antenna board" is basically the same described in the previous section with the double polarized stacked patch antenna. In the complete board the implementation of blind vias is not a a problem since the high complexity of the PCB make them mandatory. For this reason the feeding via for the patch antennas is connected only to the main patch without making necessary the isolation on the stacked patch. Another difference from the previously presented PCB, is the antenna feeding line. Since the stackup impose the presence of other substrates, the feed line can't be anymore a microstrip. A stripline structure is used for the feeding between the substrates.

A critical portion of the complete module is the transition between the Antenna and the MMIC boards. In particular, the transition between the mictostrips connected to the MMIC and the striplines connected to the antennas needs to be studied. The solution exploited in this work is illustrated in Fig.5.12(b). The structure is a coaxial cable inspired transition. The lines are connected through a RF signal vias. On its boundary the RF signal vias is confined by 4 ground connected vias. These vias act as an outer conductor of the coaxial cable allowing to achieve very low losses even at high frequencies. Finally, to have a better matching a stub is inserted. The S-parameters simulation results of the transition are reported in Fig. 5.12(c). The designed transition results shows losses of $<$ 1dB and a good matching condition ($<$ -15dB) in the band of interest.

The detailed final stackup is illustrated in Fig. 5.13. It is made by 8 metal layers. The high frequency substrate materials are the RO4350BLoPro as a core laminate

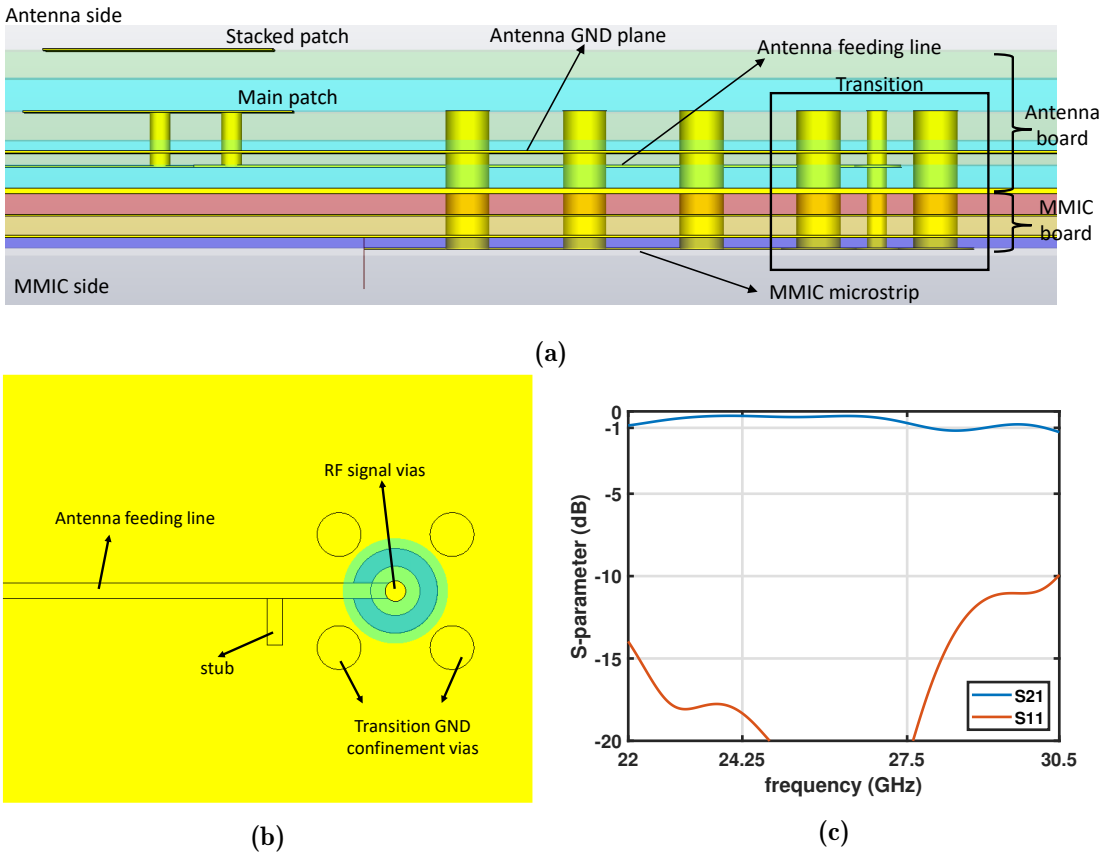

Figure 5.12. (a) Sectional view of the simulation setup for the complete antenna module, the two different section "Antenna board" and "MMIC board" are highlighted, (b) Top view of the transition from the antenna side. Only metal layers are displayed. (c) S-parameters simulation results of the designed transition.

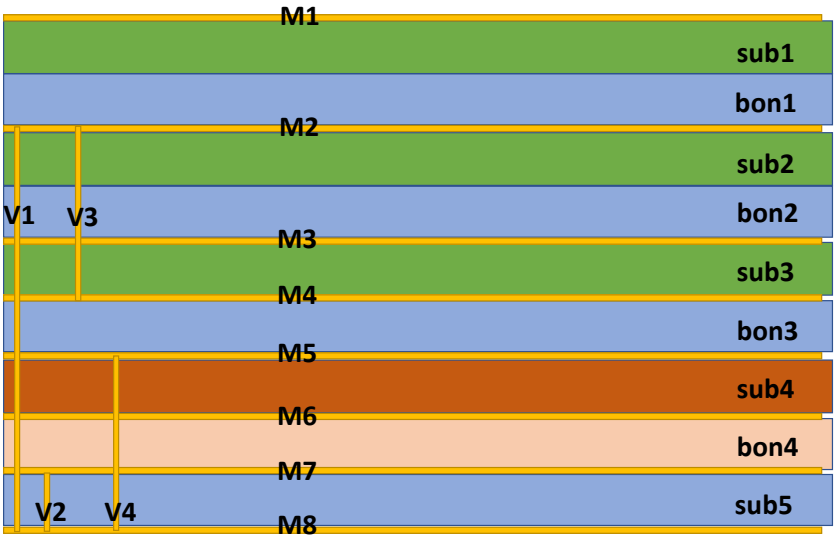

Figure 5.13. Stackup of the complete antenna module. Layers are described in Tab. 5.3.

and the RO4450F as a prepreg. The low frequency susbtrates are composed by ISOLA 370HR ($D_k = 4.23$) as a core material and the ISOLA 1080 ($D_k = 3.7$) as a prepreg. The vias connections are designed by considering the realization process. A synthetic description of the layers with material and thicknesses is provided in Tab. 5.3.

5.3.2 Complete module

The complete module PCB is illustrated in Fig.5.14. Here the metal layers seen form the antenna side and the MMIC side are shown. The board has 3 connectors. One is for the supply and the digital connections. Then, two SMP connector are used for the V pol and H pol signals. The RF signal path description when the module is in transmission configuration is the following. The high frequency signal coming from the SMP is split between the two MMICs exploiting a Wilkinson power divider. Inside the electronic devices the signal is split between the outputs and correctly changed in phase to achieve the desired beam direction. Then, through the previously described transition the RF power goes to feed the radiating patches. To keep the digital programming easier the feeding lines from the MMICs to the antennas are kept with the same length. The overall board dimensions are Wtot = 75.5mm and Htot = 28.5mm resulting in a very compact module that can be easily integrated on the car.

Layer	Name	Material	Thickness(mm)	Description
1 (TOP)	M1	Copper	0.017	Stacked patch
2	sub1	RO4350BLoPro	0.271	Stacked patch substrate
3	bon1	RO4450F	0.102 x 2	Stacked patch substrate
4	M2	Copper	0.017	Main patch
5	sub2	RO4350BLoPro	0.102	Main patch substrate
6	bon2	RO4450F	0.102 x 3	Main patch substrate
7	M3	Copper	0.017	Ground Plane
8	sub3	RO4350BLoPro	0.102	Stripline substrate
9	M4	Copper	0.017	Stripline feed
10	bon3	RO4450F	0.102 x 2	Stripline substrate
11	M5	Copper	0.035	Ground plane
12	sub4	ISOLA 370HR	0.203	LF substrate
13	M6	Copper	0.035	VDD
14	bon4	ISOLA 1080	0.152	LF substrate
15	M7	Copper	0.017	Ground plane
16	sub5	RO4350BLoPro	0.102	Microstrip substrate
17 (BOT)	M8	Copper	0.017	Microstrip feed
4-17	V1	Copper	0.2 (diam)	RF trans & GND
15-17	V2	Copper	0.2 (diam)	Microstrip confinement
4-9	V3	Copper	0.2 (diam)	Feed patches
11-17	V4	Copper	0.2 (diam)	VDD

Table 5.3. Layers description of the complete module PCB stackup illustrated in Fig.5.13.

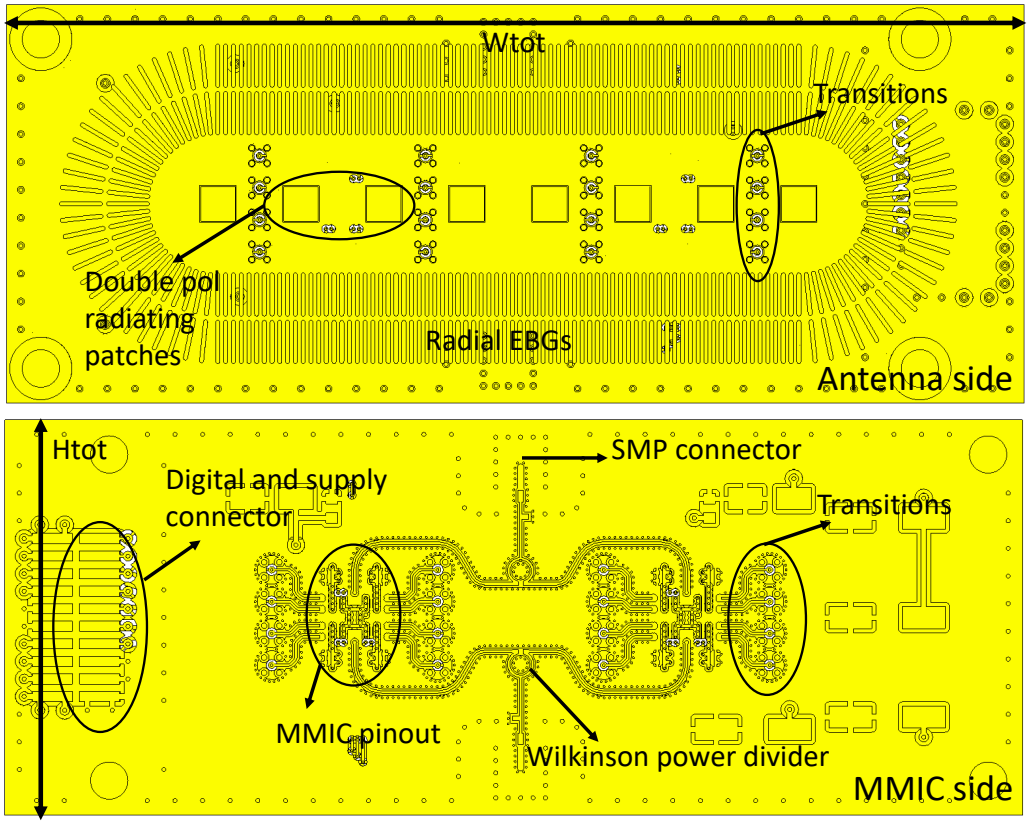

Figure 5.14. Antenna side view and MMIC side view of the complete PCB module. Only metal layers are shown. Overall dimensions are Wtot = 75.5mm and Htot = 28.5mm.

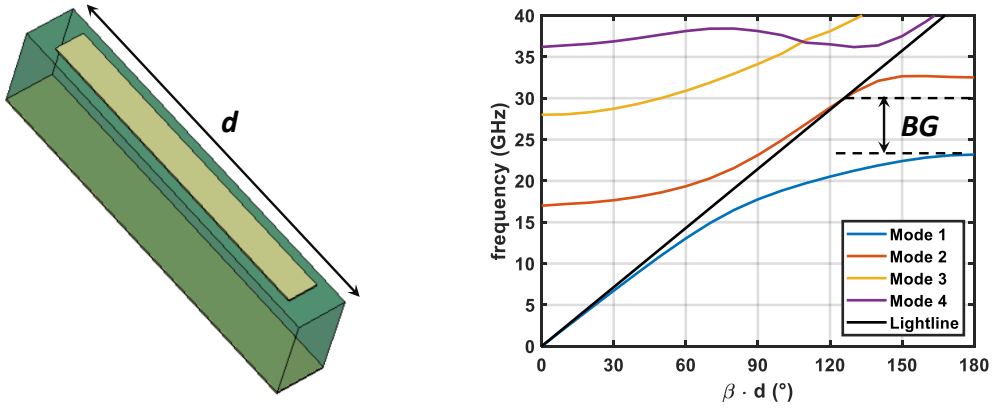

(a) (b)

Figure 5.15. (a) Simulated unit cell of the EBG structure implemented in the complete module. (b) Dispersion diagram of the second EBG structure, the obtained Band Gap from 23GHz to 30GHz is highlighted.

To suppress the surface wave propagation, also in the complete module an EBG structure is used. From Fig.5.14 it can be noticed that a different EBG design has been implemented respect to the one previously described in the radiating element design section. In fact, in the final module a resonant dipole solution has been exploited [49][50]. The simulated unit cell is represented in Fig.5.15(a). It is composed by a resonant printed line displaced along the surface wave propagation direction.The unit cell will be periodically placed around the radiating elements resulting in a "radial" distribution. Respect to the previous geometry, the main advantage of the new EBG is that it doesn't need any via connection. This allows to simplify the overall board and reduce the costs. The tuning of the structure has been performed in the same way described for the mushroom one. In Fig.5.15(b) the achieved dispersion diagram is shown. A BG from 23GHz to 30GHz is obtained. From simulations we observe that two repetitions of the structure [51] is enough to countermeasure the radiation pattern distortion.

Figure 5.16 reports the simulation results of the complete module PCB board. In Fig. 5.16(b) the ARC results for the central element of the array are shown. The antenna achieves a good matching even at the limit scanning angle case of $\phi = 45°$. The achieved realized gain at broadside direction is illustrated in Fig.5.16(b). Both the V pol and H pol, have a gain grater than 12.5dBi in the whole n258 frequency band. Respect to the results reported in Fig.5.10(b) the gain remains almost constant in all the band. This is due to the different behaviour of the two EBG structures. The difference can be noticed also in Fig.5.16(c) where the radiation

pattern on the elevation cut is reported. Here it can be observed that the patterns don't present strong distortions or differences between the polarizations even at the two limit frequencies of 24.25GHz and 27.5GHz. Finally, in Fig.5.16(d) the radiation pattern on the azimuthal cut is reported. Here, three different scanning angle at 26GHz are illustrated.

5.4 Conclusions

In this chapter a mmW antenna suitable for 5G communications in the automotive market is presented. First a study on the requirements and constrains are reported. Then a possible solution for the radiating elements alone has been described. After that the connection with the MMIC has been considered and inserted in complete antenna module, that is automotive compliant.

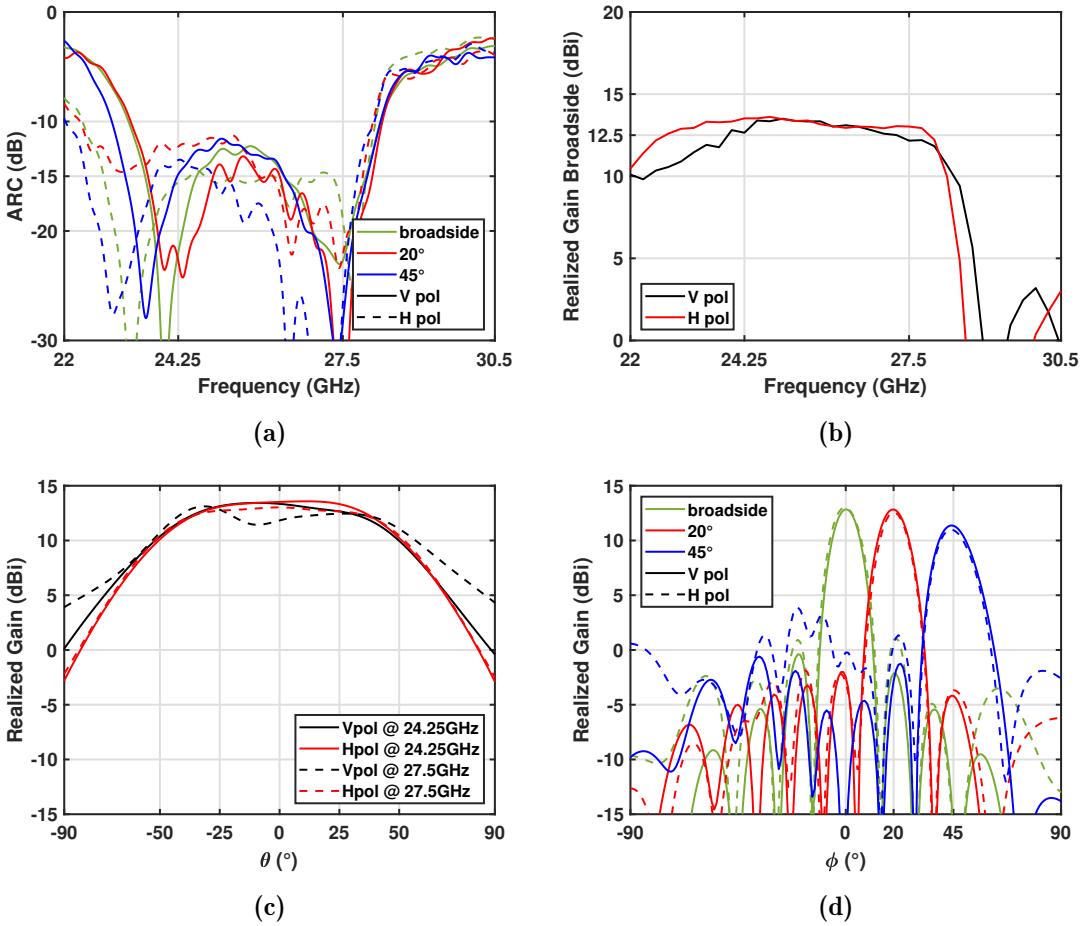

Figure 5.16. (a) Simulated ARC of the complete mmW module for both the polarization at three different scanning angles. (b) Simulated realized gain for both the polarization at broadside direction. (c) Simulation results radiation patterns at the elevation cut ($\phi = 0°$) for both the polarization at the upper and lower limit frequencies. (d) Simulation results radiation patterns at the azimuthal cut ($\theta = 0°$) for both the polarization at three different scanning angles at 26GHz.

Chapter 6

Conclusions and future developments

In this thesis modern applications for automotive antennas has been studied. In particular, it is possible to consider V2X the leading next future innovation for the car communications. In fact it can be a leading technology for the development of the Advanced Driver Assistant Systems (ADAS) or the autonomous driving. Since in modern standards the V2X transmissions can be be made through the 5G cellular network, in this work, the integration of this technology in the automotive market is mainly addressed.

First the sub6-GHz band has been analyzed. A novel low-cost 3D tin sheet radiating element has been proposed and prototyped. After that a complete sharkfin module that includes the most recent antenna functions has been described. In particular, a commercial mechanical structure and the most common automotive constraints has been considered in order to take into account a realistic environment. The module comprises a GNSS HP antenna, the 5G radiating element and one ad-hoc V2X monopole. Also this complete module has been validated through experimental measurements.

The second frequency band for the 5G is the mmW band. To gain know how in the technologies for this high frequencies, two antennas for space applications have been designed. In fact, in this market it is a well-established technology. The fist described work comprises a novel feeding system that exploits a multimodal transmission inside a waveguide. The proposed structure is based on the quasi-optical pillbox system and allows to feed antennas that need a linear source (e.g. CTS antenna, metasurfaces antennas). Its peculiarity is that it allows these structures to be illuminated by two orthogonal E-field simultaneously. The second designed antenna for space applications is a CTS antenna. This antenna topology achieves wideband and wide beam steering. In particular the proposed one, thank to a

novel E-field rotator, allows to radiates directly in circular polarization. Both of these structures are designed to be realizable with different technologies, for example metal additive manufacturing. Unfortunately they are still under fabrication and the simulation results are not be validated through measurement yet.

Finally, a mmW antenna for automotive 5G application as been considered. Since no examples are available on the market, an analysis on the standards has been conducted to extract the requirements and the constraints for the 5G in this frequency band. After that an array composed by 8 stacked patches able to radiates in double linear polarization has been designed to be realized with the low profile PCB technology. A prototype of the radiating elements alone has been fabricated and the simulations have been validated through measurements. In order to achieve a real time beam steering a complete antenna module, comprising the electronic has been considered. In particular an MMIC able to change real time the phase of the radiating element needs to be installed on the PCB. The integration between the previously designed radiating elements and the electronics leads to an increase of the dimension of the PCB board. For this reason a radiation pattern distortion due to surface waves propagation has been observed. This effect has been counteracted thanks to the exploitation of EBG structures. A complete antenna module comprising two MMICs and the antenna array has been designed and analyzed through simulations. Also for this antenna we planned to fabricate the prototype and conduct measurements in order to validate the design. Furthermore, the design of a mechanical support and a plastic radome needs to be evaluated carefully in order to not spoil the antenna radiation characteristics.

Another important future development of the projects is the study of the installation on the vehicle. In fact its positioning can affect the antenna characteristics. For this reason, usually automotive antennas are tested also in the real environment with the car travelling on the road. Typical measured performances parameters regard the full transmission system like for example the Bit Error Rate or the throughput. This type of tests can be easily done with the 5g-sub6 complete module because the infrastructure (e.g. base stations) are already present. On the other hand, for the 5G mmW frequency band is more difficult to find ready to use infrastructures. For this reason we decided to develop a full-stack module (i.e. comprising the transceiver and the modem) and realize the tests between two of our systems.

Finally it can be highlighted that the know-how acquired with the 5G technology, in particular the in the mmW band, can be useful in the automotive market also for other applications. For example, radars that works at mmWs are already present on the cars. Furthermore, satellite communications like Low Earth Orbit

(LEO) internet connection will be soon available for the consumer market [52]. Since radiation toward the sky is ideal from the roof top of a car, it is easy to imagine a internet-connected vehicle through this technology.

Bibliography

[1] "Third generation partnership project (3gpp." [Online]. Available: https://www.3gpp.org/

[2] "Spectrum for 4g and 5g," June 2020. [Online]. Available: http://www.qualcomm.com/

[3] R. Ferretti Corradi, S. Lenzini, F. Melli, A. Notari, and L. Vincetti, "3d automotive antenna for 5g and v2x communicarions," in *2021 XXXXIVth General Assembly and Scientific Symposium of the International Union of Radio Science*, 2021, pp. 1073–1076.

[4] M. O. Khalifa, A. M. Yacoub, and D. N. Aloi, "A multi-wideband compact antenna design for vehicular sub-6ghz 5g wireless systems," *IEEE Transactions on Antennas and Propagation*, pp. 1–1, 2021.

[5] "[2] e/ece/trans/505 united nations regulations, addendum n. 25." [Online]. Available: https://www.unece.org/fileadmin/DAM/trans/main/wp29/wp29regs/2013/R026r1e.pdf

[6] F. Melli, S. Lenzini, M. Cerretelli, E. Coscelli, A. Notari, and L. Vincetti, "Low cost 3d tin sheet multiband shark-fin antenna for lte mimo vehicular application," *Microwave and Optical Technology Letters*, vol. 62, no. 12, pp. 3876–3880, 2020.

[7] E. Ghafari, A. Fuchs, D. Eblenkamp, and D. N. Aloi, "A vehicular rooftop, shark-fin, multiband antenna for the gps/lte/cellular/dsrc systems," in *2014 IEEE-APS Topical Conference on Antennas and Propagation in Wireless Communications (APWC)*, 2014, pp. 237–240.

[8] S. Hasturkolu and S. Lindenmeier, "Antenna module with new wideband 5g-antenna array at 28 ghz in combination with gnss- and 4g/wlan/dsrc in automotive environment," in *2018 48th European Microwave Conference (EuMC)*, 2018, pp. 1073–1076.

[9] H. Yasin and H.Loudhaief, "Vehicle-mount antenna assemblies having covers with back tension latching mechanisms for achieving zero-gap." U.S. Patent US10 008 767, 2018.

[10] G. K. Reed and T. Shirley, "Multiband vehicular antenna assemblies." World Patent WO2016/032 624, 2016.

[11] M. G. N. Alsath and M. Kanagasabai, "Compact uwb monopole antenna for automotive communications," *IEEE Transactions on Antennas and Propagation*, vol. 63, no. 9, pp. 4204–4208, 2015.

[12] A. Michel, P. Nepa, M. Gallo, I. Moro, A. P. Filisan, and D. Zamberlan, "Printed wideband antenna for lte-band automotive applications," *IEEE Antennas and Wireless Propagation Letters*, vol. 16, pp. 1245–1248, 2017.

[13] *CST Microwave Studio*, 2019.

[14] *Cadence AWR Design Environment*, 2020.

[15] C. A. Balanis, *Antenna Theory: Analysis and Design, 4th ed.* New York: Wiley, 2016.

[16] M. Del Mastro, F. F. Manzillo, M. mierzchalski, D. González-Ovejero, P. Philippe, P. Potier, R. Sauleau, and M. Ettorre, "Circularly-polarized cts arrays," in *2019 13th European Conference on Antennas and Propagation (EuCAP)*, 2019, pp. 1–3.

[17] R. Dybdal, *Coomunication satellide antennas: system architecture, technology, and evaluation.* New York: McGraw-Hill, 2009.

[18] H. Bayer, A. Krauss, T. Zaiczek, R. Stephan, O. Enge-Rosenblatt, and M. A. Hein, "Ka-band user terminal antennas for satellite communications," *IEEE Antennas and Propagation Magazine*, vol. 58, no. 1, pp. 76–88, 2016.

[19] J.-W. Lian, Y.-L. Ban, H. Zhu, and Y. J. Guo, "Reduced-sidelobe multibeam array antenna based on siw rotman lens," *IEEE Antennas and Wireless Propagation Letters*, vol. 19, no. 1, pp. 188–192, 2020.

[20] H. Lu, Z. Liu, Y. Liu, H. Ni, and X. Lv, "Compact air-filled luneburg lens antennas based on almost-parallel plate waveguide loaded with equal-sized metallic posts," *IEEE Transactions on Antennas and Propagation*, vol. 67, no. 11, pp. 6829–6838, 2019.

[21] M. Ettorre, R. Sauleau, and L. Le Coq, "Multi-beam multi-layer leaky-wave siw pillbox antenna for millimeter-wave applications," *IEEE Transactions on Antennas and Propagation*, vol. 59, no. 4, pp. 1093–1100, 2011.

[22] J. Ruiz-García, M. Faenzi, A. Mahmoud, M. Ettorre, P. Potier, P. Pouliguen, R. Sauleau, and D. González-Ovejero, "Quasi-optical excitation of a circularly-polarized metasurface antenna at k-band," in *2020 14th European Conference on Antennas and Propagation (EuCAP)*, 2020, pp. 1–4.

[23] M. Del Mastro, A. Mahmoud, T. Potelon, R. Sauleau, G. Quagliaro, and M. Ettorre, "Low-profile cts array in pcb technology for k/ka-band applications," in

2021 15th European Conference on Antennas and Propagation (EuCAP), 2021, pp. 1–3.

[24] M. Ettorre, F. F. Manzillo, M. Casaletti, R. Sauleau, L. Le Coq, and N. Capet, "Continuous transverse stub array for ka-band applications," *IEEE Transactions on Antennas and Propagation*, vol. 63, no. 11, pp. 4792–4800, 2015.

[25] V. Mazzola and J. Becker, "Coupler-type bend for pillbox antennas," *IEEE Transactions on Microwave Theory and Techniques*, vol. 15, no. 8, pp. 462–468, 1967.

[26] D. M. Pozar, *Microwave Engineering, 4th ed.* New York: Wiley, 2013.

[27] M. Smierzchalski, F. F. Manzillo, M. D. Mastro, N. Capet, B. Palacin, R. Sauleau, and M. Ettorre, "A novel dual-polarized continuous transverse stub antenna based on corrugated waveguides - part 1: Principle of operation and design," *IEEE Transactions on Antennas and Propagation*, vol. 69, no. 3, pp. 1302–1312, 2021.

[28] ——, "A novel dual-polarized continuous transverse stub antenna based on corrugated waveguides - part 2: Experimental demonstration," *IEEE Transactions on Antennas and Propagation*, vol. 69, no. 3, pp. 1313–1323, 2021.

[29] M. Del Mastro, F. Foglia Manzillo, D. González-Ovejero, M. Smierzchalski, P. Pouliguen, P. Potier, R. Sauleau, and M. Ettorre, "Analysis of circularly polarized cts arrays," *IEEE Transactions on Antennas and Propagation*, vol. 68, no. 6, pp. 4571–4582, 2020.

[30] J. I. Volakis, *Antenna Engineering Handbook, 4th ed.* New York: McGraw Hill, 2007.

[31] W. W. Milroy, "Continuous transverse stub element devices for flat plate antenna arrays," U.S. Patent US5 483 248A, 1996.

[32] W. W. Milroy, S. B. Coppedge, and A. C. Lemons, "Variable inclinations continuous transverse stub array." U.S. Patent US6 919 854B2, 2005.

[33] F. Foglia Manzillo, M. Smierzchalski, L. Le Coq, M. Ettorre, J. Aurinsalo, K. T. Kautio, M. S. Lahti, A. E. I. Lamminen, J. Säily, and R. Sauleau, "A wide-angle scanning switched-beam antenna system in ltcc technology with high beam crossing levels for v-band communications," *IEEE Transactions on Antennas and Propagation*, vol. 67, no. 1, pp. 541–553, 2019.

[34] "Thinkom solutions, inc." [Online]. Available: https://www.thinkom.com//

[35] M. Del Mastro, M. Ettorre, and A. Grbic, "Dual-band, orthogonally-polarized lp-to-cp converter for satcom applications," *IEEE Transactions on Antennas and Propagation*, vol. 68, no. 9, pp. 6764–6776, 2020.

[36] *Ansys HFSS, High Frequency Simulation Software*, 2019.

[37] "Tr38.815," 2019. [Online]. Available: http://www.3gpp.org/

[38] "Tr38.101-2," 2019. [Online]. Available: http://www.3gpp.org/

[39] H. AlSaedi, W. M. Abdel Wahab, S. Gigoyan, R. Mittra, and S. Safavi-Naeini, "Ka-band antenna with high circular polarization purity and wide ar beamwidth," *IEEE Antennas and Wireless Propagation Letters*, vol. 17, no. 9, pp. 1697–1701, 2018.

[40] K. Wong, *Compact and Broadband Microstrip Antennas*. New York: Wiley, 2002.

[41] C.-A. Yu, E. S. Li, H. Jin, Y. Cao, G.-R. Su, W. Che, and K.-S. Chin, "24 ghz horizontally polarized automotive antenna arrays with wide fan beam and high gain," *IEEE Transactions on Antennas and Propagation*, vol. 67, no. 2, pp. 892–904, 2019.

[42] M. Mosalanejad, S. Brebels, I. Ocket, C. Soens, and G. A. E. Vandenbosch, "Stacked patch antenna sub-array with low mutual coupling for 79 ghz mimo radar applications," in *2017 11th European Conference on Antennas and Propagation (EUCAP)*, 2017, pp. 190–194.

[43] "High frequency electronics product selector guide," 2020. [Online]. Available: https://rogerscorp.com/

[44] D. Pozar, "The active element pattern," *IEEE Transactions on Antennas and Propagation*, vol. 42, no. 8, pp. 1176–1178, 1994.

[45] D. Pozar and D. Schaubert, "Scan blindness in infinite phased arrays of printed dipoles," *IEEE Transactions on Antennas and Propagation*, vol. 32, no. 6, pp. 602–610, 1984.

[46] D. Sievenpiper, L. Zhang, R. Broas, N. Alexopolous, and E. Yablonovitch, "High-impedance electromagnetic surfaces with a forbidden frequency band," *IEEE Transactions on Microwave Theory and Techniques*, vol. 47, no. 11, pp. 2059–2074, 1999.

[47] F. Zavosh and J. Aberle, "Single and stacked circular microstrip patch antennas backed by a circular cavity," *IEEE Transactions on Antennas and Propagation*, vol. 43, no. 7, pp. 746–750, 1995.

[48] I. J. Hwang, H. W. Jo, B. K. Ahn, J. I. Oh, and J. W. Yu, "Cavity-backed stacked patch array antenna with dual polarization for mmwave 5g base stations," in *2019 13th European Conference on Antennas and Propagation (EuCAP)*, 2019, pp. 1–5.

[49] M. Ettorre, S. Bruni, G. Gerini, A. Neto, N. Llombart, and S. Maci, "Sector pcs-ebg antenna for low-cost high-directivity applications," *IEEE Antennas and Wireless Propagation Letters*, vol. 6, pp. 537–539, 2007.

[50] N. Llombart, A. Neto, G. Gerini, and P. de Maagt, "Planar circularly symmetric ebg structures for reducing surface waves in printed antennas," *IEEE Transactions on Antennas and Propagation*, vol. 53, no. 10, pp. 3210–3218, 2005.

[51] ——, "1-d scanning arrays on dense dielectrics using pcs-ebg technology," *IEEE Transactions on Antennas and Propagation*, vol. 55, no. 1, pp. 26–35, 2007.

[52] "Starlink, spacex." [Online]. Available: https://www.starlink.com/